GIANT MOLECULAR COMPLEXES AND OB ASSOCIATIONS.
I. THE ROSETTE MOLECULAR COMPLEX

LEO BLITZ[1]
Columbia University

AND

PATRICK THADDEUS
Goddard Institute for Space Studies
Received 1979 October 22; accepted 1980 April 14

ABSTRACT

This is the first of three articles which present systematic observations of the molecular complexes related to OB associations in the third galactic quadrant. In this article, we present CO observations of the Rosette molecular complex which is associated with Mon OB2. The complex is extended along the galactic plane, has a maximum extent of ~100 pc, and shows a striking interaction with the Rosette Nebula. The complex appears to have a well defined boundary, and it is likely that the complex is no more than ~20% larger in any one dimension than the extent defined by our lowest contour. The molecular gas appears to be embedded in an H I cloud with a mass comparable to the molecular mass. We estimate the molecular mass to be $1.3 \times 10^5 M_\odot$, and the inferred volume density to be ~30 cm^{-3}. The complex possesses an overall velocity gradient of 0.20 km s^{-1} pc^{-1}. At high resolution the CO appears to be very clumpy. Evidence for very recent star formation appears at the site of unusual CO self-reversal, but not at the position of maximum CO emission.

Subject headings: clusters: associations — interstellar: molecules — nebulae: individual — stars: formation

I. INTRODUCTION

Most massive stars are born in OB associations (Roberts 1957; Miller and Scalo 1978) in which the youngest members are often still associated with the dark material from which they formed (Blaauw 1964). Millimeter-wave and infrared observations have shown that the gaseous component of these dark clouds is primarily molecular, and they often show evidence of continuing star formation (e.g., Werner, Becklin, and Neugebauer 1977). Because CO is the most abundant molecule with a microwave spectrum and because the ratio of CO to H_2 is approximately constant (Thaddeus 1977), it is a good tracer for the molecular gas related to the OB associations. We have made CO observations of the molecular complexes related to three OB associations toward the galactic anticenter. This paper presents the results for Mon OB2 (related to the Rosette Nebula). The results for Mon OB1 (related to NGC 2264 and the Cone Nebula) and CMa OB1 will be presented in subsequent papers. These associations are particularly good objects to study because (1) they are relatively spatially isolated, (2) there is little foreground or background molecular gas to confuse the interpreta-

tion of the results, and (3) the number of O and B stars in these associations is representative of the range found in most galactic OB associations (e.g., Blaauw 1964).

In this paper we outline the observational techniques and methods of analysis (§ II) used for all of the complexes. These are discussed in detail in the appendices. In § III we present observations of the Rosette molecular complex (Mon OB2), in § IV we discuss the results in terms of the properties of the complex, and in § V the relation of the complex to the process of star formation. Section VI is a summary of the results.

II. OBSERVATIONS

a) Equipment

Each complex was observed in the $J = 1 \rightarrow 0$ transition of CO and ^{13}CO. The observations were made in 1976–1977, and three instruments were used: the 1.2 m telescope at Columbia University in New York, the 5 m telescope at the Millimeter Wave Observatory[2] (MWO)

[1]Presently at the Radio Astronomy Laboratory, University of California, Berkeley.

TABLE 1

TELESCOPE PARAMETERS[a] RELEVANT TO THE OBSERVATIONS

Observatory	Aperture (m)	Beam Size FWHM (arcmin)	Instantaneous Bandwidth (km s^{-1})	Velocity Resolution (km s^{-1})	SSB Noise Temperature (K)	Limiting rms Sensitivity (K)
Columbia	1.2	8	104	2.6	900	0.3
MWO	5	2.3	26	0.65	1800	0.5–0.8
NRAO	11	1	67[b]	0.26	600	0.7
			333[b]	1.3		0.3

[a] At 115 GHz.
[b] Observations were made using two filter banks simultaneously.

near Fort Davis, Texas, and the 11 m telescope at the National Radio Astronomy Observatory[3] (NRAO) near Tucson, Arizona. The relevant parameters of each telescope are summarized in Table 1.

Each complex was observed with full beamwidth sampling using the 1.2 m telescope. To obtain increasingly higher spatial and velocity resolution, selected areas were observed with the 5 m and 11 m telescopes. A detailed description of each instrument and the observing procedures which were used are given in Appendix A. In order to compare the calibration at all three telescopes, velocity integrated intensities of several regions were corrected for differences in spatial resolution. The intensities generally agreed to within 25%.

b) The Extent of the Complexes

We have mapped the full extent of the CO emission related to each complex to a limiting sensitivity of 1 K-MHz at the 1.2 m telescope. The results were extrapolated to zero intensity to estimate the amount of undetected gas below the sensitivity limit of the observations (see Appendix B for details). The extrapolations imply the following: (1) If each complex were observed at an arbitrarily high sensitivity, the average linear dimension of each complex would increase by no more than ~20%. The complexes therefore appear to have relatively well defined sharp boundaries. (2) The intensity gradient in the outer regions is reasonably constant from one complex to another (see Appendix B) and is given by

$$\log A = -0.16(\pm 0.02)T + C, \qquad (1)$$

where A is the projected area in pc^2 within a given intensity contour, T is the contour level in K-MHz, and C is the extent of the complex defined by the zero intensity contour in pc^2. The constancy of this relation from complex to complex may be indicative of a fundamental property of giant molecular complexes.

c) The Mass of the Complexes

The mass of each complex was determined by an LTE analysis of the CO profiles using ^{13}CO as a tracer for the molecular gas, and applying Dickman's (1978) value for the ratio of $H_2/^{13}$CO (see Appendix C for details). The ^{13}CO emission is generally much weaker than the CO emission, however, and in the regions where ^{13}CO was below the sensitivity limits of the observations, CO was used as a tracer for the H_2. The mass obtained in the regions where ^{13}CO was observed is the directly observed mass M_{OBS} of the complex. We designate the region where the ^{13}CO was not observed as the CO halo, and the estimated mass in this region M_{HALO}. Similarly, the unseen mass below the sensitivity limit of the CO observations is designated M_{UNS}. The uncorrected mass of the complex is $M_{COMP} = M_{OBS} + M_{HALO} + M_{UNS}$.

Corrections to the mass estimates are required because (1) the lines were, in general, not fully resolved in frequency at the 1.2 m telescope, and (2) Dickman's $H_2/^{13}$CO ratio may be an underestimate in the dense cores of molecular complexes. These corrections are described in Appendix C. Both tend to revise the mass estimates upward. The total mass of each complex after the corrections are applied is designated M_{TOT}.

Although the absolute values of M_{TOT} are uncertain by a factor of ~2, the *relative* masses of the complexes are likely to be more accurate by half an order of magnitude. Each of the three giant complexes was observed with the same instrument in a consistent manner. The errors in the relative masses are therefore due primarily to calibration uncertainties, and uncertainties in the distance to each complex. We estimate that the total uncertainties in the relative masses are ~25–50%.

III. RESULTS

a) Overall Properties

We have found a large molecular cloud complex which appears to be interacting with the Rosette Nebula and is therefore associated with the cluster NGC 2244 and the Mon OB2 association. Figure 1 (Plate 9) shows
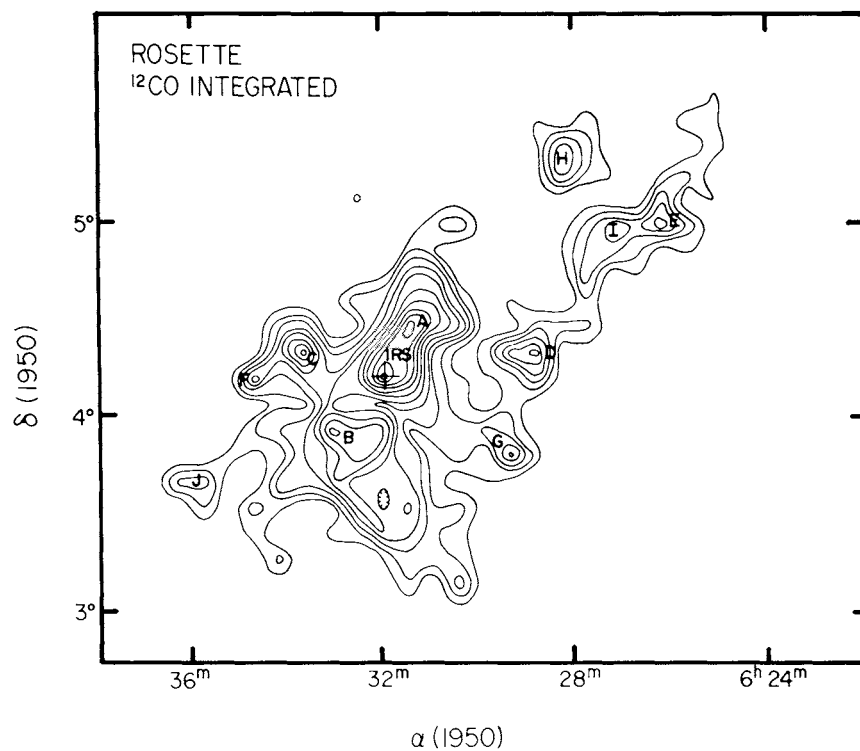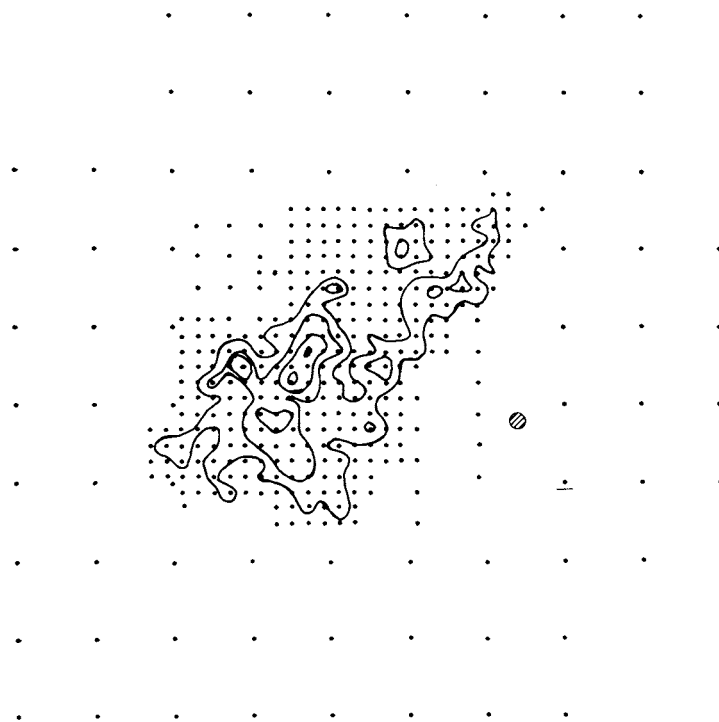
FIG. 2a

FIG. 2b

FIG. 2.—(a) Map of the integrated CO emission from Mon OB2 showing the locations of the maxima listed in Table 2a. The contour interval is 1 K-MHz. (b) The sampling for the Mon OB2 molecular complex. Each dot represents a sample point. Outside of the lowest contour, the only emission greater than 1 K-MHz occurs at the underlined point. This point coincides with the isolated dark cloud L1633.

the emission from this complex observed with the 1.2 m telescope superposed on the red Palomar Observatory Sky Survey (POSS) plate of the region. Apparently, the molecular gas has been largely destroyed in the direction of the Rosette by the ionizing and dissociating radiation, and it is obvious why previous attempts to find molecular clouds associated with the Rosette have failed (Turner 1969; Zuckerman *et al.* 1970; Milman *et al.* 1975).

As Figure 1 shows, the Rosette molecular complex is elongated roughly parallel to the galactic plane. The maximum angular extent of the complex is 3°.5, which corresponds to 98 pc at an assumed distance of 1600 pc. Observations at higher spatial and frequency resolution show a ridge of emission (the Monoceros Ridge— indicated by an arrow in Fig. 1) which is aligned with a prominent dust lane in the southeast corner of the Rosette. A precipitous decline in CO intensity occurs on the side of the dust lane facing the center of the H II region. Although some optical emission extends beyond this ridge, the most intense emission is adjacent to the dust lane and the associated molecular material. It appears likely that the Monoceros Ridge is where the ionization front is in direct contact with the molecular gas.

There is likely to be little additonal CO emission related to Mon OB2 other than what is shown in Figure 1. This is evident from Figure 2b, which shows the sampling used for the 1.2 m observations. No other emission was found except at the underlined position, which corresponds to the small isolated dark cloud L1633. The velocity of L1633 is 9.5 km s^{-1} compared to the center-of-mass velocity found for the Rosette of 14.3 km s^{-1}. This velocity difference and the spatial iso-

lation of L1633 seem to indicate that it is unrelated to the Rosette complex.

The structure of the molecular complex can be seen clearly in Figure 2a, which shows the CO data from Figure 1 plotted with a contour interval of 1 K-MHz.

Eleven distinct maxima are evident and following the designations of Figure 2a, their positions and intensities are listed in Table 2A. Although the maximum integrated emission is from peak IRS (which is coincident with the unusual infrared source GL-961), the highest antenna temperature is found 20′ to the northwest at peak A. It will be shown below that this difference is due to the large width of the line at peak IRS. The structure apparent in Figure 2 occurs on all scales down to the limiting resolution of these observations; many of the maxima shown in Figure 2 will be seen to consist of several subcondensations. These are listed in Table 2B and discussed in §§ III*b*. Figure 3 shows integrated ^{13}CO emission greater than 1 K-MHz from the Rosette complex observed with the 1.2 m telescope. The most intense emission comes from peak A, and no separate distinct feature occurs at peak IRS. The sampling for the ^{13}CO observations is also shown.

The velocity structure of the CO is quite complex. In addition to numerous clumps which have relative velocities of several km s^{-1} (see below), the entire complex has a velocity gradient which is shown in Figure 4. Each panel in this figure represents the CO emission in a particular spectrometer channel. There is a clear progression of the velocity in each channel (weighted by the intensity) from the southeast to the northwest (Fig. 4f), a direction roughly parallel to the galactic plane. Figure 5 is a plot of velocity versus longitude

TABLE 2A

EMISSION MAXIMA IN THE MONOCEROS OB2 MOLECULAR CLOUD[a]

Source	α(1950)	δ(1950)	T_A^* ^{12}CO (K-MHz)	T_A^* ^{13}CO (K-MHz)	Positional Uncertainty[b] (arcmin)
IRS[c].....	6^{h}31^{m}58^s	4°15′30″	11.4	1.6	±1
A[d].......	6 31 28	4 28 00	10.7	3.4	...
B[e].......	6 33 04	3 56 00	8.0	1.9	±10
C	6 33 36	4 20 00	8.0	2.0	±10
D[d]	6 28 48	4 20 00	6.3	0.5	...
E[d]	6 26 08	5 00 00	5.4	0.9	...
F.......	6 34 40	4 12 00	5.4	...	±10
G	6 29 38	3 58 00	5.0	...	±3
H	6 28 16	5 16 00	4.7	...	±10
I[d]	6 27 12	5 00 00	4.5	...	...
J........	6 35 44	3 40 00	3.5	...	±10

[a] From 1.2 m data.

[b] Positional uncertainty of 10′ indicate position is from CSST observations, of 3′ from MWO observations, of 1′ from NRAO observations.

[c] Position is that of maximum CO self-reversal.

[d] Composed of several sources. See Table 2B.

[e] May be composed of more than one source.

TABLE 2B

INDIVIDUAL CLUMPS IN THE MONOCEROS OB2 MOLECULAR COMPLEX

Clump	Subpeak	$\alpha(1950)$[a]	$\delta(1950)$[a]	V_{LSR}[b] (km s^{-1})	T_A^* ^{12}CO (K)	T_A^* ^{13}CO[c] (K)
A1.........	1	6 31 28^{s}[d]	4°28′00″[d]	15.5[e]	21.0	6.4
	2	6 30 48	4 33 00	16	13.4	2.5
	3	6 31 18	4 33 00	16	13.3	2.4
	4	6 31 28	4 20 30	16	12.0	1.7
A2 ("EAR").	1	6 30 38	4 38 00	14	10.1	2.6
	2	6 30 48	4 48 00	10	9.8	4.1
	3	6 31 18	4 43 00	14	9.1	1.3[f]
	4	6 31 18	4 40 30	12	8.9	...
	5	6 30 58	4 45 30	12	8.8	2.1
A3.........	1	6 31 38	4 20 30	10	6.8	2.2[g]
A4.........	1	6 30 52	4 38 00	39.6[e]	4.0	...
A5.........	1	6 30 48	4 38 00	22.0[e]	4.0	...
IRS........	1	6 31 58	4 15 30	12.9[e,h]	9.6	5.0
B1.........	1	6 31 38	4 05 30	12	6.1	...
D1	1	6 28 58	4 23 00	14	7.9	...
D2	1	6 28 28	4 30 30	16	6.8	...
D3	1	6 28 38	4 20 30	12	7.0	...
	2	6 29 48	4 20 30	13	5.7	...
I1	1	6 26 38	4 58 00	15	13.3	<0.6
	2	6 26 58	4 58 00	15	11.8	<1.0
I2	1	6 27 28	4 55 30	19.5	10.1	1.7
	2	6 27 48	5 00 30	18	8.0	...
I3	1	6 27 48	4 45 30	17	10.0	2.6
E1.........	1	6 26 08	5 00 30	19	10.5	...
E2.........	1	6 25 58	5 00 30	17	9.3	...
I4	1	6 27 08	4 55 30	13	4.7	...
G1	...	6 29 38	3 58 00	16	10.3	...

[a] All positions ±3′ except as indicated.

[b] All velocities ±0.7 km s^{-1} except as indicated.

[c] Peak ^{13}CO temperatures occur at the velocity at which the ^{12}CO peak occurs except as noted.

[d] Positional error ±1′.

[e] Velocity is ±0.3 km s^{-1}.

[f] Max T_A^* $^{13}CO = 2.5$ K at $V_{LSR} = 12$ km s^{-1}.

[g] Max T_A^* $^{13}CO = 3.3$ K at $V_{LSR} = 11$ km s^{-1}.
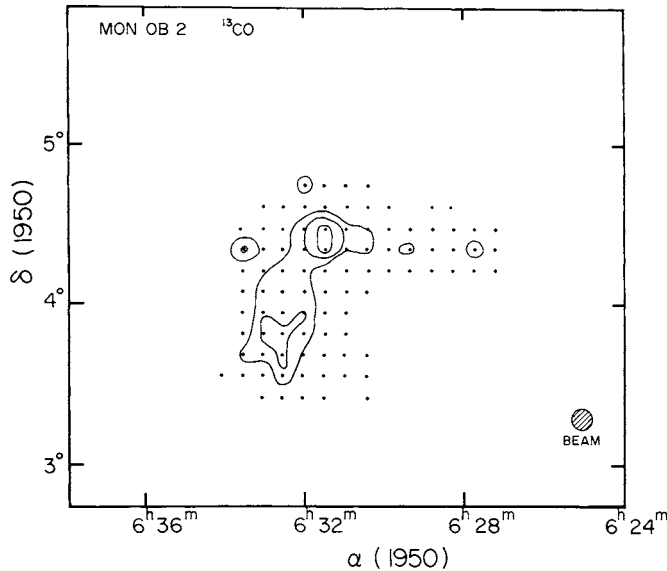
[h] ^{13}CO velocity; see Table 4.

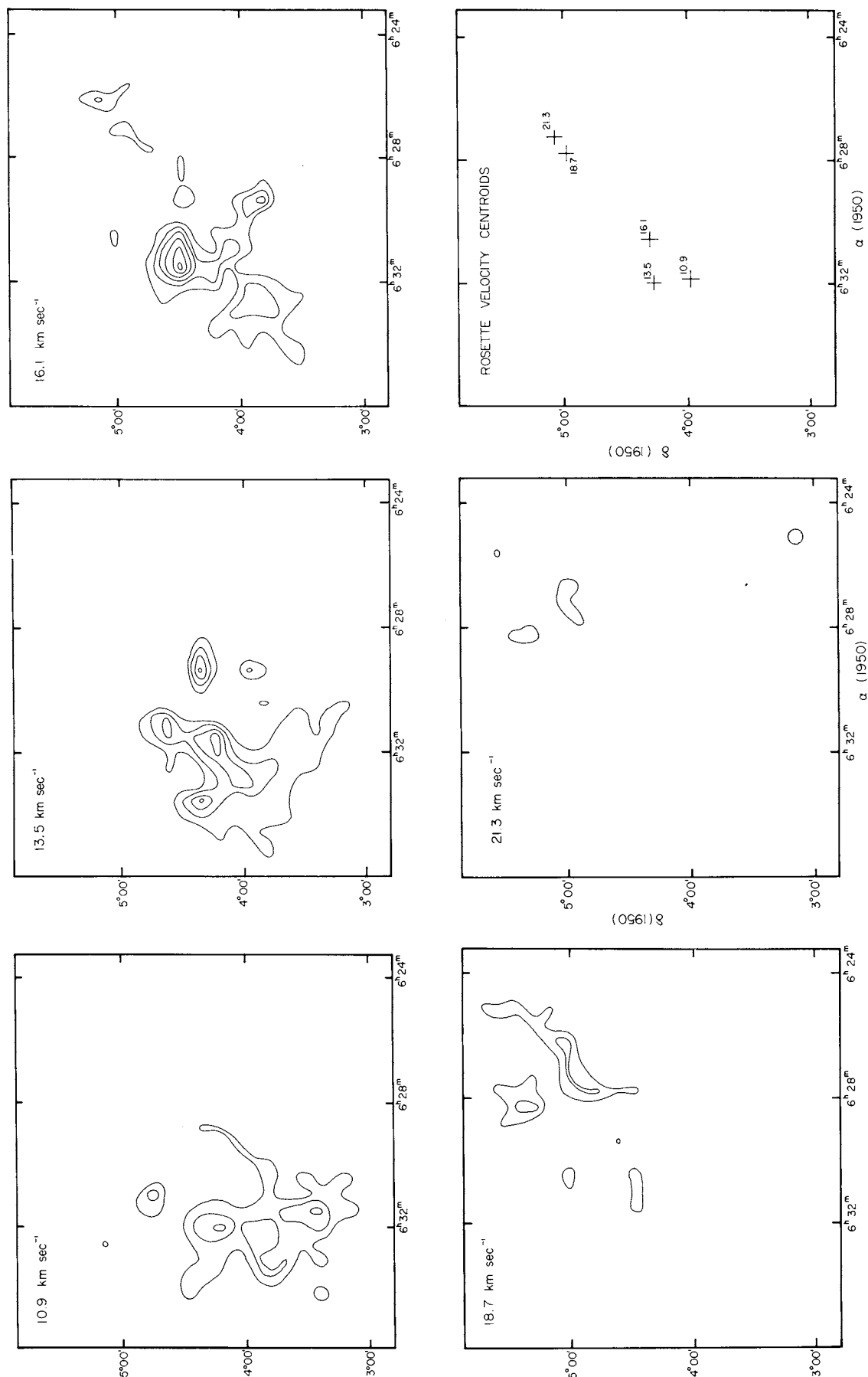FIG. 3.—Map of the ^{13}CO antenna temperature from the Mon OB2 complex. Each contour is 1 K-MHz.

FIG. 4.—The velocity structure of the Mon OB2 complex. Panels 4a–4e show the emission in individual successive spectrometer channels. The contour levels are 1 K. Panel 4f shows the location of the intensity weighted centroid of the emission centroid from the southeast to the northwest with increasing velocity. Note the progression of the emission at each velocity.
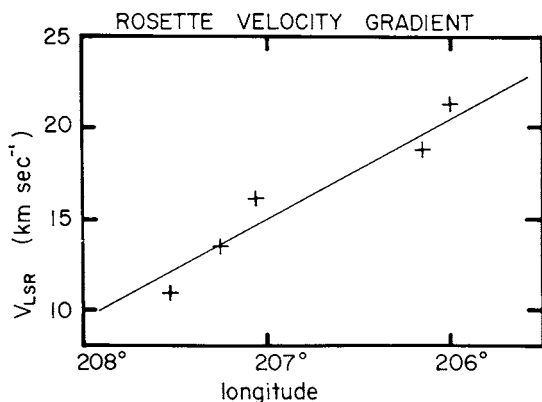
ROSETTE VELOCITY GRADIENT

FIG. 5.—Plot of the velocity of the CO emission as a function of the location of the velocity centroid projected onto the galactic plane showing the velocity gradient across the complex.

from the data used to construct Figure 4. The velocity gradient across the complex is 0.20 km s^{-1} pc^{-1}. If this gradient is due to rotation, the period is 3.1×10^7 yr and the projected rotation axis is opposite to that expected from differential galactic rotation. The magnitude and sense of the velocity gradient are similar to that found by Kutner *et al.* (1977) for the giant molecular complex associated with the Orion Nebula.

Calculating the mass of the complex as described in Appendix C, we find that the total mass of the complex is 1.3×10^5 $M_\odot$. We find that the mass of the molecular gas below the limiting sensitivity of the observations (M_{UNS}) is less than 25% of the total mass of the complex. It appears therefore that we have detected nearly all of the molecular gas related to the complex. The mass fraction of gas with a ^{13}CO column density greater than 1.0×10^{16} cm^{-2}, (f_{core}), is 0.07. Therefore, even if there were large deviations from Dickman's ratio in the high-density regions, the total mass of the complex would not be significantly changed. At a dis-

TABLE 3
PROPERTIES OF THE ROSETTE MOLECULAR COMPLEX

Distance...................	1600 pc[a]
Mean LSR velocity..........	14.3 km s^{-1}
Velocity gradient............	0.20 km s^{-1} pc^{-1}
Maximum linear extent	98 pc
Projected area	2.51 square degrees, 1.95×10^3 pc^2
Mean antenna temperature ...	8.95 K-km s^{-1}
Mean column density[b].......	2.4×10^{21} cm^{-2}
Mass:	
M_{OBS}....................	2.5×10^4 $M_\odot$
M_{HALO}..................	5.3×10^4 $M_\odot$
M_{UNS}...................	2.3×10^4 $M_\odot$
M_{COMP}..................	10.1×10^4 $M_\odot$
f_{CORE}...................	0.074
M_{TOT}	1.3×10^5 $M_\odot$
Mean H$_2$ number density	30 cm^{-3}

[a]Walker 1976.
[b]Using $N(H_2)/N(^{13}CO) = 5 \times 10^5$ throughout complex.

tance of 1600 pc (§ IV*a*) the projected area of the complex corresponds to a projected surface area of 1.95×10^3 pc^2. Assuming that the volume is given by the area raised to the 1.5 power, the mean density of the complex is 30 cm^{-3}.

A summary of the large scale properties of the Rosette complex is given in Table 3.

b) *Detailed Structure*

We have made high-resolution observations with the 5 m telescope in the vicinity of peaks IRS, A, B, D, E, and I. Figures 6 and 7 are maps of CO and ^{13}CO at a resolution of 2′.5 in that part of the Rosette complex where the CO emission is most intense, a region which includes peaks IRS, A, and B. Figure 6 shows considerable spatial structure which is not resolved with the 1.2 m telescope. This structure is especially apparent in Figure 7 which shows the results of ^{13}CO observations in this region made with the 5 m telescope. Because ^{13}CO is optically thin throughout most of the complex (when $\tau_{^{13}CO}$ is calculated under the assumption of LTE), the maxima in Figure 7 are indicative of density enhancements. We conclude that the molecular gas in this region and in other regions we have observed at high resolution is quite clumpy.

The emission features observed with the 5 m telescope are listed in Table 2*b*. We have tabulated these features as follows: We identify a particular feature as a clump if it has a well-defined velocity or a smooth velocity gradient. Each clump is given a letter prefix corresponding to the nearest peak in Figure 2. In some cases, several maxima occur within a particular clump; these are identified as subpeaks in Table 2B. Clumps A4 and A5 were found using the 11 m telescope. Both are small, only a few arcmin in diameter. Their high velocities indicate that they may be background objects. We will present arguments in § IV, however, why we believe them to be part of the Rosette complex.

The emission apparent in Figures 6 and 7 possesses a rich velocity structure. This can be seen in Figure 8 (Plates 10–12) which shows the peak emission (regardless of velocity) as well as the emission detected in spectrometer channels corresponding to 10.3, 12.3, 13.7, and 15.7 km s^{-1} superposed on the red POSS plate of the region. These velocities were selected for plotting because most of the maxima observed with the 5 m telescope occur at or near these velocities. The position of maximum CO emission from the complex is shown by an asterisk in all of the panels, and the position of GL-961 is shown with a cross.

i) *The Ear*

A notable optical feature of the Rosette Nebula is a network of dark dust lanes in the form of an ear, which is identified in Figure 8*a*. Figures 8*b*–8*f* show two rather striking positional coincidences. First, there is a hole in the CO emission which corresponds to the
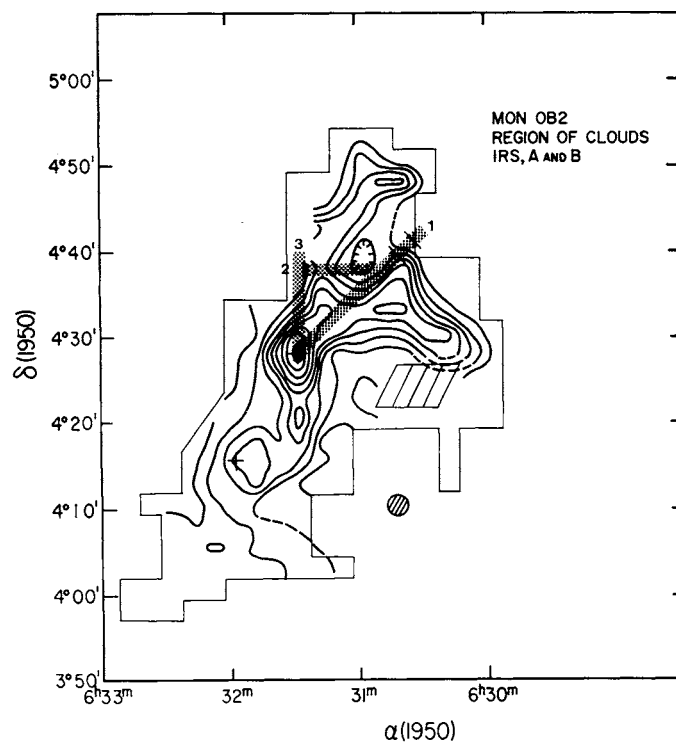
FIG. 6.—Map of the peak CO antenna temperature in the region where the emission is most intense from observations at the 5 m telescope. Within the boundaries shown by the light outlines, sampling was every beamwidth. The contour interval is 2 K, and the lowest contour is 3 K. Dashed contours are uncertain. No data were taken in the region of the hatched parallelogram. The shaded lines marked 1–3 indicate the extent of the observations made with the 11 m telescope. The tick marks on strip 1 indicate the positions where the observations cross the Mon Ridge. The cross marks the position of GL-961.
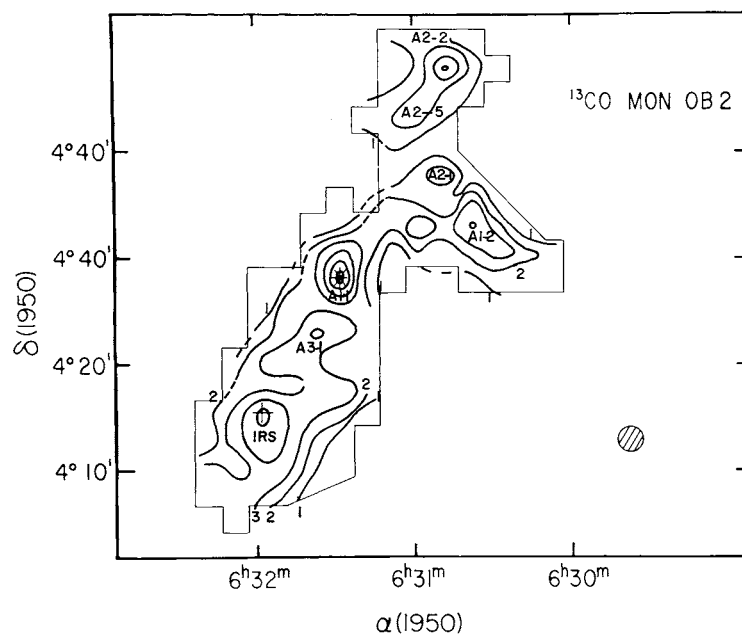

FIG. 7.—Map of peak ^{13}CO antenna temperature in the region of most intense CO emission from observations with the 5 m telescope. The region surveyed is shown by the light boundary; within the boundary, sampling was every beamwidth. The beam size is given by the shaded circle. The contour interval is 1 K, and dotted contours are uncertain. The cross marks the position of GL-961; the asterisk, the position of maximum CO emission. The various maxima are designated because they correspond to the CO clumps listed in Table 2B.
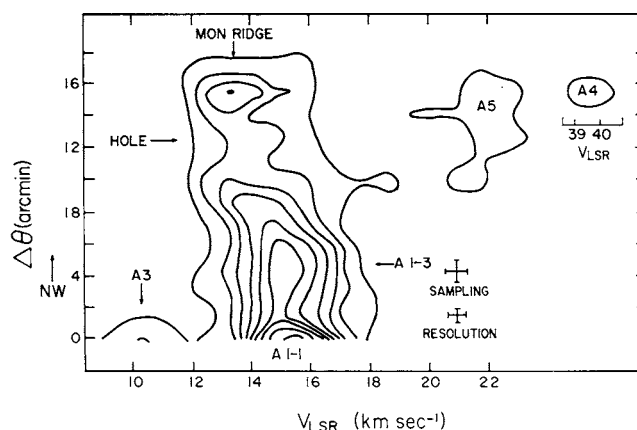
FIG. 9.—Position-velocity diagram of the CO emission along cut 1 of Fig. 6 from data collected at the 11 m telescope. The intensity gradient between positions offset 16′ and 18′ northwest of A1-1 corresponds to the region between the two tick marks along cut 1 in Fig. 6. The data were smoothed to a resolution of 250 KHz and were sampled every 300 KHz. The decrease in the emission near the position marked "Hole" is the location along cut 1 near the CO emission minimum.

increase in optical emission at the center of the Ear (seen most clearly in Fig. 8b). Second, the CO clump A2 is very sharply peaked along the semicircular dust lane which defines the easternmost portion of the Ear.

If the CO emission related to the Ear comes from a single clump, it is in the form of a shell $\sim$15′ in diameter corresponding to 7 pc at the distance of the Rosette. The CO possesses a smooth velocity gradient which increases from north to south along the semicircular portion of the Ear. If the gradient is due to rotation, the projected axis points nearly west, and the implied angular velocity is 0.8 km s^{-1} pc^{-1} (corresponding to a period of 9×10^6 yr), 5 times greater than the value derived for the complex as a whole.

The lane that forms the southwestern part of the Ear corresponds to the Monoceros Ridge. Observations along a line from peak A1-1 across the Monoceros Ridge as well as two other lines across clumps A1 and A2 were made with the 11 m telescope. The extent of these cuts is shown by the heavy lines in Figure 6; each cut is numbered. Along cut 1, between the points indicated, the peak CO emission goes from 8 K to being undetectable (< 1.5 K) in 2′, which attests to the sharpness of the ridge. The gradient in the emission can be seen in Figure 9, a position-velocity diagram made along cut 1, at a velocity of $\sim$14 km s^{-1} between positions which are 16′ and 18′ northwest of peak of A1-1. Clumps A3, A4, and A5 are visible in Figure 9, and the location marked "Hole" corresponds to the CO minimum related to the Ear. Along cut 2, the CO emission drops to $\sim$2K near the Ear hole and could be even less at the center.

ii) IRS

Another noteworthy feature in the Rosette complex is the infrared source GL-961. Although no optical

feature is evident at the position of this source, a small ($\sim$30″) cometary nebula lies less than 1′ from the infrared position (Cohen 1973). At the position of GL-961, we have found an unusual CO line profile which is shown in Figure 10. This profile is a 60 minute integration which was kindly obtained by A. A. Stark with the 7 m telescope at the Bell Telephone Laboratories, and shows the CO and ^{13}CO spectra plotted to the same scale. Note that the ^{13}CO antenna temperature actually exceeds the CO temperature over a small velocity range near the maximum self-reversal.

CO self-reversal is an uncommon phenomenon; only seven other examples have been reported. These are ρ Oph (Encrenaz, Falgarone, and Lucas 1975), W3 (Dickel *et al.* 1975), NGC 1333 (Loren 1976), NGC 2071 (Lada and Gottlieb, unpublished observations 1974), Mon R2 (Kutner and Tucker 1975), LkHα 101
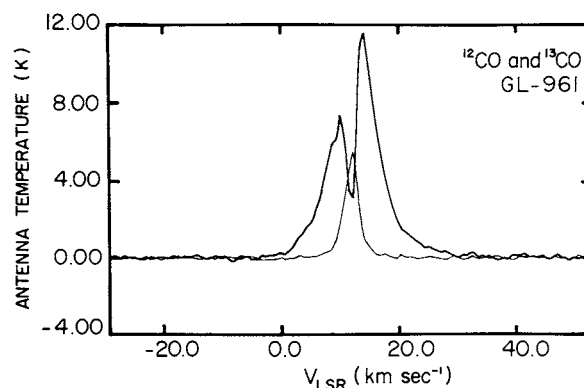

FIG. 10.—Profiles of CO (*heavy line*) and ^{13}CO(*fine line*) at the position of GL-961 showing the strong self-reversal in the CO line. Note the extensive wings from -5 to $+35$ km s^{-1}. The spectra are 1 hour integrations obtained by A. A. Stark using the 7 m telescope at the Bell Telephone Laboratories.

(Knapp *et al.* 1976), and Cep A in Cep OB3 (Sargent 1977). Three features make the GL-961 spectrum unusual. (1) All previously reported self-reversed CO lines show a marked asymmetry about the absorption minimum (Snell and Loren 1977) and a small (0.8 km s^{-1}) displacement of the ^{13}CO peak from the CO minimum. With the exception of NGC 2071, the stronger of the two CO peaks and the displacement of the ^{13}CO peak occur shortward of the CO dip. In this case, the sense of the asymmetry is reversed. (2) The depth of the self-reversed feature is much deeper than in any of the other sources, with an intensity of 2 K at the center. The self-reversed feature is also much narrower than in any of the other previously reported lines. (3) The source shows extremely broad line wings. Emission is apparent from a velocity of about -6 km s^{-1} to 35 km s^{-1}, a range of 41 km s^{-1}. None of the other self-reversed lines show such a large velocity spread, but this may be due in part to the high sensitivity and spatial resolution used for the GL-961 observations.

The extent of the CO self-reversal is at least 7′, which corresponds to 3.3 pc at the distance of the Rosette. This can be seen in Figure 11, which is a plot of the ratio of the mean antenna temperature of the primary and secondary CO peaks to antenna temperature at the CO dip. The plot is made from data taken at the 11 m telescope smoothed to 250 kHz resolution. At all positions where the ratio exceeds 2, the intensity at the dip
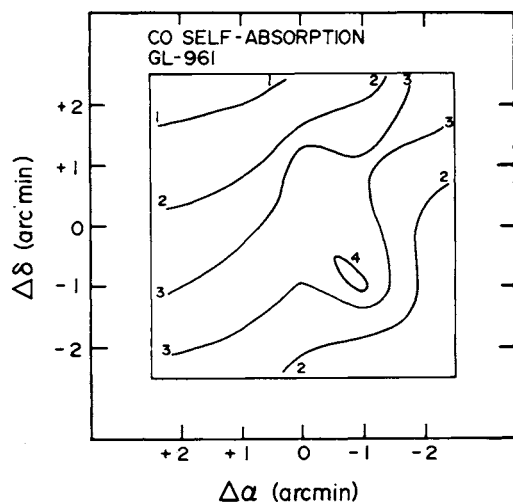
TABLE 4

OBSERVED PARAMETERS FOR GL-961[a]

	T_a^* (K)	V_{LSR} (km s^{-1})
Primary ^{12}CO peak	8.3	14.1±0.13
Secondary ^{12}CO peak ..	5.0	10.8±0.13
^{12}CO dip...........	1.5	12.0±0.26
^{13}CO peak..........	3.8	12.9±0.13
HCO$^+$ peak	0.50	13.47±0.16
HCN peak..........	0.35	13.4±0.5

	ΔV (FWHM)[b] (km s^{-1})	
^{12}CO	8.0±0.2	
^{13}CO	2.7±0.2	
^{12}CO dip[c]	1.5±0.2	
HCO$^+$	2.7±0.2	
HCN	2.6±0.2	

[a] CO parameters are from observations at the 11 m NRAO telescope. HCO$^+$ and HCN parameters are from 7 m Bell Laboratories telescope.
[b] All ΔV measured from 7 m Bell telescope data.
[c] Full width measured at the mean of the intensity of the secondary peak and minimum.

is less than that of both the primary and secondary peaks. Note that the self-reversal is extended along an axis roughly parallel to the major axis of the elongated Mon OB2 complex. The most important parameters for the line at the position of GL-961 are given in Table 4. The value given for the width of the self-reversed feature (the dip) is measured at the mean of the intensity of the secondary maximum and the minimum.

Another dip in the CO spectrum which occurs at a velocity of 10.4 km s^{-1} is evident at a number of positions. Of the positions searched, this feature is strongest 2′.8 northwest of GL-961. Like the main dip, the feature is spatially extended and has a diameter of at least 4′, but it occurs primarily to the north and west of the main dip. The ^{13}CO data were too noisy to determine whether this second feature is indeed a self-reversed line or whether it results from two separate clouds along the line of sight.

Spectra of GL-961 at the frequency of HCO$^+$ ($J=1 \rightarrow 0$) and HCN ($J=1 \rightarrow 0$) were obtained by A. A. Stark at a resolution of 0.16 and 0.50 km s^{-1}, respectively, with the 7 m telescope at the Bell Telephone Laboratories. Neither line shows evidence of self-reversal (which is also true of the ^{13}CO line). The ^{13}CO, HCN, and HCO$^+$ lines all have the same width; however, the velocity of the peak of the ^{13}CO emission is different from that of HCN and HCO$^+$. All three peaks have velocities which are different from the CO peak and the CO dip.

The width of the CO line shows a strong dependence on the spatial resolution with which it is observed. At 2′.3 resolution, the FWHM of the CO line is 5.1 km s^{-1},

FIG. 11.—The spatial distribution of the CO self-reversal toward GL-961. The contours indicate the value of the function $[T^*(13.8)+T^*(10.7)]/2T^*(12.0)$ where $T^*(x)$ is the corrected antenna temperature at x km s^{-1}. For lines which are not self-reversed, the value of the function is expected to be about unity. If the value exceeds 2, the line shows a pronounced central minimum. For the purposes of plotting this figure, the spectra were smoothed to a resolution of 0.65 km s^{-1}, and were sampled every 0.78 km s^{-1}.

and at $1\overset{.}{.}6$ the width is 8.0 km s^{-1}. A CO spectrum in the $J=2\rightarrow1$ line of CO was obtained by Carlson at Bell Laboratories at a resolution of $0\overset{.}{.}8$; the line width is 11.3 km s^{-1}. The ^{13}CO line width shows no such variation. This implies that the high-velocity gas in the wings is not extended, and is probably not resolved even at the highest resolution. Furthermore, because ^{13}CO shows no line width variation, the CO wings are likely to be optically thin, as is true for the wings in the CO peak in Orion (Wannier and Phillips 1977).

iii) The Arm

Figure 1 shows an arm of CO along the western periphery of the Rosette complex extending to the northwest from the main molecular complex. We have mapped the CO in the vicinity of peaks E and I in this "Arm" with the 5 m telescope; the results are shown in Figure 12 (Plates 13–15). The figure shows a map of the peak emission in this region (regardless of velocity) and the emission in spectrometer channels corresponding to 15, 17, and 19.5 km s^{-1} superposed on the red POSS plate of the region. As in Figures 6 and 7, we note the intricate spatial and velocity structure of the region.

Although there are dust clouds seen in projection against the optical nebula in the vicinity of the Arm, the correspondence between the optical features and the CO clouds is not as good as they are near the Ear. There is, however, a good correspondence between the 19.5 km s^{-1} feature of cloud I2 (12-1) and a diffuse dark cloud. Emission from ^{13}CO was measured at several positions in this region, and the velocities show a good correlation with CO velocities. The various features seen in Figure 12 therefore seem to be evidence for clumpy structure in this region.

IV. DISCUSSION

a) The Stellar Association

The Mon OB2 association is a rich grouping of early type stars containing 13 stars of spectral type O9.5 and earlier (Johnson 1962; Morgan *et al.* 1965; Turner 1976). The cluster NGC 2244 forms the core of the OB association and contains five O stars which excite the Rosette Nebula. Riddle (1972) and Turner (1976) have concluded that the association contains at least two subgroups of different ages, and that the cluster NGC 2244 represents the most recent epoch of star formation. The overall morphology of the region and the ages of the stellar subgroups are consistent with the notion that massive star formation has proceeded sequentially in the Mon OB2 association (e.g., Blaauw 1964; Elmegreen and Lada 1977). We will show below, however, that the structure of the Rosette complex indicates that the details of the star formation process may be different from that discussed by Elmegreen and Lada.

Turner's (1976) spectrophotometric analysis of the stars in Mon OB2 yields a distance of 1600 pc to the association. From the CO observations, we derive a kinematic distance of 1.4 kpc using the rotation curve of Blitz, Fich, and Stark (1979), in good agreement with Turner's value. Because the molecular gas is subject to random motions of $\sim$7 km s^{-1} (Blitz, Fich, and Stark 1979), the photometric distance is probably more reliable than the kinematic distance, and will therefore be adopted as the distance to the molecular complex.

b) The Molecular Complex

Perhaps the most surprising result in Table 3 is the value of the mean volume density of H$_2$ molecules derived from the CO observations. This density is an order of magnitude smaller than the value usually derived for molecular clouds (e.g., Turner 1974; Dickman 1978). Subsequent papers in this series will show that this value is typical of the three complexes we observed. Our low value for the mean H$_2$ density can be understood if the complex is clumpy.

We illustrate the clumpiness by considering the objects listed in Table 2b. The derived size, mass, and volume density for a number of the clumps is given in Table 5. The diameter given is the mean of the largest and smallest projected extent of the clump (observationally defined as the extent of a given velocity component—measured by T_L^{12}) recognizable above the noise. Clumps for which the boundaries are poorly determined are indicated. Where extensive ^{13}CO observations exist, the mass is found by obtaining the mean column density, applying Dickman's value of $N(\text{H}_2)/N(^{13}\text{CO})$, and multiplying by the surface area. Volume densities are derived assuming spherical clumps. If ^{13}CO was observed only at the CO peak, the clump is assumed to be uniform and spherical, in which case the mass is given by $\frac{2}{3}\pi R^2 N(\text{H}_2)$, where R is the radius of the clump. The masses and densities in Table 5 are lower limits because they occur in that part of the complex with the largest column densities. $N(\text{H}_2)/N(^{13}\text{CO})$ is likely to be higher here than Dickman's value (cf. Appendix C). In any event, Table 5 shows that the mean clump density probably varies from about several hundred to $\sim$1000, in spite of a mean density for the complex of $\sim$30.

Most of the clumps have densities consistent with values derived from observations of other molecular clouds (e.g., Turner 1974; Dickman 1978). The clumps have sizes which vary by an order of magnitude and masses which vary by 2.5 orders of magnitude. Most of the mass in the regions observed, however, appears to come from clumps 5–10 pc in diameter with masses of 10^3–10^4 $M_{\odot}$. The volume filling factor for the clumps is $\sim$0.1–0.3, which implies a projected surface filling factor near unity. This result is consistent with the observation that there are no places where the CO

TABLE 5

MASSES OF THE CLUMPS IN THE MONOCEROS OB2 COMPLEX

Cloud	Diameter (pc)	$\langle N_{H_2} \rangle^a$ $\times 10^{21}\,cm^{-2}$	Mass ($M_\odot$)	Mean n_{H_2} (cm^{-3})	Remarks
A1..........	10	6.1	8000	340	...
A2 ("EAR").	6.5	1.8	800	83	Apparent shell with 2.5 pc thickness
A3..........	5	3.9	800	270	No ^{13}CO observations; $\tau_{13CO} =$ 0.35 assumed
A4..........	1.5	1.2	20	250	No ^{13}CO observations; $\tau_{13CO} =$ 0.35 assumed
A5..........	3	1.2	80	125	...
IRS.........	8^b	3.7	3000	250	...
G1	8^b	1.9	1000	82	...
I1	5	<0.46	<100	<33	$T_L^{13}\infty < 0.6$
I2	6^b	1.3	400	78	...
I3	6^b	2.2	700	140	...

^{a}Assumes $N(H_2)/N(^{13}CO) = 5 \times 10^5$.
^{b}Uncertain; could be somewhat larger.

emission is undetectable within the boundary of the complex defined by the lowest contour in Figure 1.

Raimond (1966) has observed the 21 cm line in the vicinity of Mon OB2 with the 25 m Dwingeloo telescope at a resolution of $0°.56$ and 2.1 km s^{-1}. He found an H I cloud that he calls feature C which is coincident with the molecular complex shown in Figure 1. The H I cloud is apparent above the galactic background from an LSR velocity of 0.5 km s^{-1} to 25.8 km s^{-1}. The largest column depths occur between velocities of ~5 and 22 km s^{-1}, roughly equal to the velocity range observed in CO. Figure 13 shows the half-peak column density contour for the H I gas superposed on the lowest contour of Figure 1. The spatial coincidence is rather striking.

The single cross in Figure 13 marks the position of maximum H I column density $(2.9 \times 10^{21}\,cm^{-2})$; the asterisk marks the position of maximum H$_2$ column density $(1.1 \times 10^{22}\,cm^{-2})$. Raimond obtained a mass for cloud C of $1.5 \times 10^5\,M_\odot$ assuming a distance of 1390 pc; at a distance of 1600 pc the mass is $2.0 \times 10^5\,M_\odot$, comparable to the derived H$_2$ mass. The ionized mass of the Rosette Nebula has been found to be $1.1 \times 10^4\,M_\odot$ (Menon 1962; Bottinelli and Gouguenheim 1964) and is therefore a small fraction of the mass of the complex. Raimond estimated that the total stellar mass in Mon OB2 is ~6000 $M_\odot$, also a small fraction of the total gaseous mass. The total mass of the entire complex is therefore ~$4 \times 10^5\,M_\odot$.

The atomic gas appears to be well mixed (at the resolution of Raimond's observations) with the molecular gas. If the atomic gas envelops the molecular complex and is segregated from the molecular material, the atomic gas should show limb brightening at positions

just outside of the molecular cloud (a characteristic of optically thin shell structures), but this does not appear to be the case at any velocity. Another possibility is that the atomic gas is a foreground or background sheet which abuts the molecular gas. Although this possibility cannot be ruled out, the similar morphology of the atomic and molecular gas shown in Fig. 13 suggests a more intimate relationship.
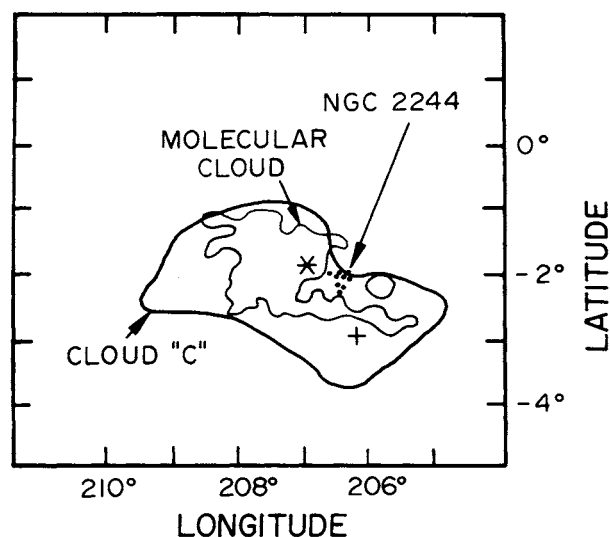

FIG. 13.—Map of the lowest contour of Fig. 2 superposed on the half-peak column density contour of Raimond's (1966) H I cloud "C." The coordinates are galactic latitude and longitude. The cross marks the position of maximum H I column density and the position of the asterisk marks the position of maximum H$_2$ column density (A1-1).

Burton, Liszt, and Baker (1978) have shown that some self-absorbed H I profiles are well correlated with molecular emission, suggesting that the molecular clouds contain residual cold atomic gas which is well mixed with the molecular gas. They find that, in the regions they observed, the ratio of the column densities $N_{H_2}/N_{H_I} \sim 500$. The full extent of Raimond's cloud C is roughly 5–10 times greater than the projected area of the molecular complex. The volume of the H I cloud is therefore likely to be $\sim$10–30 times greater than the volume of the CO complex. Taking into account the differences in H_2 to H I mass, $N_{H_2}/N_{H_I} \approx 15$–75 in the molecular complex if the atomic and molecular gas are well mixed: an order of magnitude larger than the value of Burton *et al.* It appears, then, that there is considerably more warm H I within the molecular complex than cold H I.

A possible explanation for the warm H I gas is that it occurs primarily in the region within the complex *between* the individual clumps discussed above. The minimum temperature of the intercloud gas in the complex is determined by the velocity dispersion of the individual clumps of $\sim$1–2 km s^{-1}. If the individual clump motions are not to be very short-lived ($\ll 10^6$ yr), the sound speed of the intracomplex gas must be $\sim$1–2 km s^{-1}, which implies a minimum kinetic temperature for the atomic gas of 100–400 K.

c) The Relationship to the Rosette Nebula

The Rosette Nebula is one of the best examples of the clear interaction between a molecular complex and an H II region. The ionizing radiation from the stars and the stellar winds appear to have effectively destroyed most of the molecules within the projected area of the optical nebula. In addition to the partial shell of molecular gas which appears to envelop the southern and western part of the Rosette, there is some evidence for a shell of H I which has been swept up by the H II region: Raimond's data show distinct H I peaks at three positions just outside the boundary of the Rosette. We conclude that NGC 2244 was probably formed from what was once a more extensive molecular complex. The location of the molecular cloud and the Rosette are anticorrelated, an indication that the orientation of the H II region to the molecular cloud is roughly perpendicular to the line of sight. Another indication comes from the sharpness of the Monoceros Ridge (§ III*b*). If the radial extent of the ridge is the same as its apparent length ($\sim$ 15'), cloud A1 and the Rosette Nebula are oriented about 80° to the line of sight.

Radio continuum observations by Menon (1962) and by Bottinelli and Gouguenheim (1964) show a close correspondence between the optical and radio emission. The radio continuum peak occurs in a region adjacent to the Monoceros Ridge, apparently confirming that this is one of the locations where the ionization front is impinging on the molecular complex.

The mean velocities of the stars, the ionized gas, and the molecular gas in the vicinity of the Rosette all agree well. Riddle (1972) has found that the mean LSR velocity of NGC 2244 is 21 ± 3 km s^{-1}. Three independent observations of Hα from the nebula indicate a velocity for the ionized gas of 19 ± 5 km s^{-1} (Courtès, Cruvellier, and Georgelin 1966; Miller 1968; Smith 1968). The CO observations in the immediate vicinity of the Rosette (see Fig. 5) indicate a mean velocity of 18.7 ± 1.5 km s^{-1}. There is therefore no significant difference in the velocities of the stars, the H II region, or the molecules in the immediate vicinity of the Rosette.

The nature of the interaction between NGC 2244, the Rosette Nebula, and the preexisting gas has been discussed by many authors. Minkowski (1949) showed that the radiation from NGC 2244 is sufficient to ionize the Rosette, and that the gaseous mass is $\sim 10^4 M_\odot$. There are numerous small globules seen in projection in the northeast quadrant of the nebula, some of which are as small as 3" ($\sim$4500 AU). Herbig (1974) has shown that these globules have teardrop shapes with sharp edges and symmetry axes directed toward the center of the cluster. He argues that the globules are the detached remains of elephant trunk structures and that the region is in the process of being swept clear of interstellar material. Schneps, Ho, and Barrett (1980) have found CO associated with a number of the globules. The globules may therefore be the dense fossil remnants of a once more extensive molecular cloud.

The results of Schneps *et al.* indicate that a number of the Rosette globules have velocity gradients of $\sim$2–3 km s^{-1} pc^{-1}, and ages of $\sim$3–5$\times 10^5$ yr. This age is consistent with the dynamical age of the Rosette (2–6 $\times 10^5$ yr, Mathews 1967), and from the expansion age of the central cavity ($\sim 1 \times 10^5$ yr, Smith 1973). The age of the H II region is thus likely to be the same as the age of the brightest cluster members and is probably $\sim 3 \times 10^5$ yr.

The expansion of the central cavity may be related to the acceleration of the dark globules. Smith (1973) has observed the 5007 Å [O III] line towards the Rosette and found that the ionized gas is expanding at $\sim$20 km s^{-1}. Fountain, Gary, and O'Dell (1979) found similar results from Hα measurements. Schneps, Ho, and Barrett (1979) have found that the CO related to the globules is blue shifted by $\sim$20 km s^{-1} from the mean CO velocity of 18.7 km s^{-1} in the immediate vicinity of the Rosette. Mathews (1966, 1967) proposed three mechanisms for the formation of the central cavity: (1) condensation into stars, (2) stellar winds from NGC 2244, (3) radiation pressure on grains frozen into the plasma. Neither (1) nor (3) is consistent with the observations of the supersonic [O III] and Hα lines. Further evidence against (1) comes from molecular observations in the vicinity of infrared sources interpreted to be protostellar or neostellar (recently formed) objects. These infrared sources are invariably associated

with local *maxima* in the gas density and not local minima (see e.g., Werner, Becklin, and Neugebauer 1977).

Using the models of Dyson (1973), Smith (1973) has shown that a stellar mass loss rate of $1-2\times10^{-6}$ $M_\odot$ yr^{-1}, giving rise to wind with a velocity of 2000 km s^{-1}, could produce the expansion of the central cavity. Hutchings (1976) has measured the mass loss rate from the O5 star HD 46150 to be 1.5×10^{-6} $M_\odot^{-1}$. This star is very close to the geometrical center of the cavity, and is therefore likely to be responsible for it.

In addition to the Rosette, there are two other H II regions, S280 and S282, which are near the edge of the molecular complex. The northernmost extent of S280 appears to be partially obscured by the dust in the molecular complex, but neither H II region appears to be interacting with the molecular complex (see Blitz 1978 for details) and therefore will not be considered further.

The general picture that emerges from these observations is the following: within the Mon OB2 molecular complex, the stars which are now part of NGC 2244 began to form and disrupt the molecular material. With the formation of the O stars about 3×10^5 years ago, the Rosette Nebula began to form and expanded until it reached its present size. The H I and H$_2$ gas which surrounded the stars was ionized, forming the optical nebula. A thin shell of gas swept up by the shock front is now visible as an H I shell just outside the Rosette, and in the molecular emission surrounding the Rosette on all sides but the north and northeast. Stellar winds (possibly in combination with radiation pressure on the grains) from the O stars in NGC 2244 (particularly HD 46150) have caused the central regions of the nebula to become depleted and have given rise to the expansion of the central cavity.

d) The Ear

The Ear feature is closely related to a ridge of CO emission with a large, smooth velocity gradient. We have identified the molecular emission as a single entity (cloud A2) because of the smoothness of the velocity gradient (see Blitz 1978 for details) and the contiguous optical appearance of the dust lane. The feature might nevertheless consist of several fragments.

The morphology of the region suggests that the Ear is expanding. The lack of CO at the center of the Ear corresponds closely to an increase in the optical emission and suggests that the Ear may be a miniature version of the Rosette itself. That is, early type stars in the center of the Ear caused the ionization and dissociation out to a radius of ~2.5 pc, and the shell of CO is matter being swept up behind the shock. Because the molecular shell is incomplete in the west toward the center of the Rosette, it may be that the ionization fronts of the Rosette and the Ear feature have joined where the molecular emission disappears.

The hypothesis that the Ear is an H II region–molecular shell structure provides a natural explanation for the high-velocity clouds A4 and A5. Although they may be background objects, both occur within the Ear feature, and may be dense fragments which have been accelerated by the rocket effect (see e.g., Spitzer 1978), or by stellar wind pressure. No early type star has yet been identified, however, which could account for the morphology of the region.

e) IRS

The full extent of the cloud in which the infrared source GL-961 is located is not well determined from the Columbia and MWO observations, but the area of greatest interest is the immediate vicinity of the CO self-reversal. The self-reversal could be due to a very cold (~2 K) cloud in front of the warm IRS cloud, but this would imply that the self-absorption maximum occurs within 1' of the ^{13}CO peak purely by chance. Furthermore, CO self-absorption was not observed elsewhere in this complex. It seems reasonable to conclude that the CO self-absorption is related to the temperature, density, and velocity field of a single cloud and that the phenomenon of self-reversal is related to the presence of the infrared sources, because all of them appear to be centered on infrared sources. Blitz and Lada (1979) have noted that of the eight known examples of CO self-reversal, five show the presence of H$_2$O maser emission, although GL-961 is one of the sources without such emission. Because maser emission from dark clouds, and infrared sources in dark clouds is generally thought to be an indicator of incipient star formation (see, e.g., Lada 1980), the phenomenon of CO self-reversal appears to be intimately related to the star formation process.

An unusual feature of the CO emission related to GL-961 is the very broad line wings. The 40 km s^{-1} wings are similar to the broad CO wings associated with the BN–KL region (Zuckerman, Kuiper, and Rodriguez-Kuiper 1976; Kwan and Scoville 1976), but the GL-961 wings are weaker and are not seen over as large a velocity range. If the wings in both sources are due to the same phenomenon, the observed difference between them may be due only to the different distances to both objects. Because the region giving rise to the broad Orion wings is probably not resolved with the 1' NRAO beam, if the wings in both sources have the same intrinsic intensity and the same spatial extent, beam dilution would make the wings in GL-961 appear about one-tenth as intense, just what is observed. In any event, the broad wings are much more localized than the $\gtrsim7'$ extent of the self-reversal, and were detected only at the position of the infrared source.

The infrared source GL-961 appears to be the site of very recent star formation, and it may be protostellar (Harvey, Campbell, and Hoffman 1977). The source was investigated by Cohen (1973), who found that the

luminosity and infrared spectrum of the source is similar to the Becklin-Neugebauer (BN) object. GL-961 has a color temperature of 725 K (Cohen 1976), a 2–200 μm luminosity of 5500 $L_\odot$ (Harvey, Campbell, and Hoffman 1977), and a 2.2–18μm luminosity of 1600 $L_\odot$ (Cohen 1973). By comparison, the BN object has a 1.65–20μm luminosity of 1500 $L_\odot$, and a color temperature of 530 K (Becklin, Neugebauer, and Wynn-Williams 1973). Harris (1976) searched unsuccessfully for a compact H II region around GL-961, although Simon, Simon, and Joyce (1979) detected relatively strong Bα emission. If GL-961 is like the BN object, it is probably a recently formed B star, and the lack of a detectable radio H II region is not surprising.

In order to reconcile the apparently large optical depths at 100 μm with the optical emission form the reflection nebula associated with GL-961, Harvey, Campbell, and Hoffman (1977) postulated that the dust distribution around the infrared source is asymmetric and may be in the shape of a nearly edge-on disk. This conjecture is consistent with the spatial distribution of the self-reversal shown in Figure 11, although the extent of the self-reversal is considerably larger than the scale of the model of Harvey *et al*.

In addition to the high-velocity wings, GL-961 may be the source of the large-scale motion of the IRS molecular cloud. Comparing the sense of the asymmetries of the CO line profiles with the analysis of Leung and Brown (1977), we infer that the molecular cloud is *expanding* with a maximum velocity of $\sim$0.8 km s^{-1} (the velocity difference between the ^{12}CO dip and the ^{13}CO peak). If this interpretation is correct, the expansion energy is $\sim$1.7$\times$10^{46} ergs. The infrared source radiates this much energy in 25 years. Therefore, even if the efficiency of the conversion of luminous to kinetic energy is very small, the luminosity of GL-961 appears to be sufficient to power the expansion of the IRS molecular cloud.

The infrared and radio observations of GL-961 suggests the following model: a compact infrared source, possibly protostellar, has recently formed in the CO cloud IRS. Mass outflow from the star gives rise to the broad emission wings seen in the CO which probably extend less than 0.2 pc (30″) from the central source. The stellar wind is responsible for heating the gas and dust in the immediate vicinity of the star ($<$10″ in order to be consistent with the small angular size of 100 μm emitting region observed by Harvey *et al*.). The luminous energy of the source has been converted in part into kinetic energy which is the source of the large-scale expansion of the molecular cloud which envelops GL-961.

f) CO Peak A1-1

The most intense CO emission in the Mon OB2 complex occurs at the peak A1-1. Because strong CO peaks are often indicators of recent star formation such

as infrared sources and H$_2$O masers (see, e.g., Lada 1980), it is reasonable to suspect that this peak, too, results from the stellar or prestellar heating of dense molecular gas. To test this hypothesis, the source was observed using the 2 mm H$_2$CO line which is thought to require high densities ($\gtrsim$10^5 cm^{-3}) for its excitation because of its large dipole moment. Using the 4.9 m telescope at the MWO, no H$_2$CO emission was found to 0.5 K, the 3 σ noise limit of the observations.

The source was also observed using the 130 cm IR telescope at Kitt Peak in collaboration with D. Y. Gezari and R. R. Joyce. The observations were made at 5 and 10 μm using a He-cooled In-Sn bolometer. A 12″ entrance aperture was used with a nutating secondary giving a 20″ throw. No emission was found to a flux level $\sim$1/10 of that observed for GL-961. The observations were made in the daytime by offsetting from GL-961, and there is some doubt about the absolute pointing accuracy. Blitz and Lada (1979) have also searched a 4′ diameter around A1-1 for H$_2$O maser emission and could find none to a 5 σ upper limit of 6 Jy. Evidently, there are no signs of recent star formation near this source.

One of the reasons for this could be that A1-1 is in the very early stages of collapse and has not had time to form an appreciable core. The gravitational energy released by the collapse could be heating the embedded dust, raising it to a temperature of $\sim$100–300 K, which would make the source emit infrared radiation most strongly at 100–300 μm. Temperatures significantly higher than 300 K appear to be ruled out by the lack of 10 μm emission from A1-1. This source is therefore a good candidate for far-infrared observations.

V. STAR FORMATION

Riddle (1972) and Turner (1976) discussed the ages of the stars in Mon OB2. They both find that the association contains at least two subgroups differing in age, and that the cluster NGC 2244 represents the most recent epoch of star formation. Because NGC 2244 is an unevolved O cluster, its age is not known. However, an upper limit of 3$\times$10^6 yr can be estimated for the age of the O stars (Stothers 1972) because of the presence of an O4 star on the main sequence. Both Riddle and Turner found that the early type stars centered on the northern Monoceros group (Riddle 1972), which are extended roughly as far as the Monoceros Loop supernova remnant centered about 2° northwest of the Rosette, form another subassociation with at least one evolved member. This implies that the subgroup age is $\sim$5$\times$10^6 yr. Riddle found evidence for a third subgroup, but his observations were not sufficiently extensive to confirm this. Turner found that a very extended subgroup $\sim$10° in diameter is also present which contains the two Cepheid variables T Mon and CV Mon. In this subgroup the earliest type star on the main sequence has a $(B-V)_0$ of -0.273, which

implies that the age of the subgroup is $\sim 1.5 \times 10^7$ yr. Using the theoretical period age relation of Kippenhahn and Smith (1969), Turner found that the ages of T Mon and CV Mon are 2×10^7 and 5×10^7 yr, respectively, if both are crossing the instability strip for the second time. In the unlikely event that CV Mon is crossing the strip for the first time, its age is 2.5×10^7 yr.

The stars in Mon OB2 conform to Blaauw's (1964) description of the structure of many of the OB associations within 1 kpc of the Sun. That is, there are three subassociations which have diameters that increase with age; the youngest of these is most closely associated with the molecular material. The oldest has an age of $\sim 1.5 \times 10^7$ yr and a diameter of 280 pc; the second oldest, an age of $\sim 5 \times 10^6$ yr and a diameter of ~ 150 pc; and the youngest, NGC 2244, an age of $< 3 \times 10^6$ yr and a diameter of 25 pc. As suggested by Blaauw, the youngest stars in Mon OB2 are most intimately associated with the material from which the stars formed. Although there is no direct evidence as yet that GL-961 marks the first appearance of a new subassociation, if the star is protostellar (Harvey, Campbell, and Hoffman 1977), it is surely younger than any of the very massive stars in NGC 2244.

Two possible mechanisms for initiating the most recent epochs of star formation in Mon OB2 are (i) a supernova explosion or (ii) the expansion of an H II region (Elmegreen and Lada 1977). The only apparent supernova remnant in the vicinity of GL-961 is the Monoceros Loop. The remnant is most likely to be at the distance of Mon OB2 (see Blitz 1978 for details), but the shock front (Kirschner, Gull, and Parker 1977) would just be reaching the edge of the molecular complex. The supernova shock could not therefore be responsible for the formation of either GL-961 or NGC 2244.

What if the Elmegreen-Lada mechanism were responsible for the formation of GL-961? As discussed above, Raimond's (1966) results show evidence for an atomic hydrogen shell just outside that boundary of the nebula, and Figure 2 shows evidence for a similar molecular hydrogen shell. GL-961 is located, however, $\sim 30'$ or 15 pc from the Monoceros Ridge, which is where the ionization front appears to be interacting with the molecular complex. This distance is much greater than the distance by which the shock front is likely to have preceded the ionization front into the molecular complex. The formation of GL-961 was therefore probably not triggered by the Elmegreen-Lada mechanism.

The clumpiness of the Rosette complex (and the other complexes in this series of papers) suggests that another mechanism may be responsible for the formation of massive stars in OB associations: implosion of the dense clumps. An ionization front which expands into a nonuniform medium will travel more quickly in regions of lower density. If an ionization front encounters a dense clump, it should rapidly envelop the clump. Clumps which survive for sufficiently long times will therefore be subjected to an implosion caused by the high pressure inside the ionization front. This potentially important effect has not been considered in any treatments of externally triggered star formation.

VI. SUMMARY

We have found a large (~ 100 pc) previously unknown molecular complex related to the Rosette Nebula and Mon OB2. We have detected most of the emission from this complex, the mass of which is $\sim 1.3 \times 10^5$ $M_\odot$. The Rosette complex shows a marked interaction with the optical nebula, and is likely to be oriented nearly perpendicular to the line of sight relative to the H II region. The ionization front appears to be interacting with the molecular complex along the Monoceros Ridge. The complex has a very clumpy structure with a mean H_2 density of ~ 30 cm^{-2}, and typical densities in the clumps of ~ 100–1000 cm^{-3}. The complex possesses an overall velocity gradient of 0.20 km s^{-1} pc^{-1}.

The entire complex is embedded in a large cloud of atomic hydrogen with a mass comparable to the mass of the molecular complex. At the resolution of the 21 cm observations, some of the H I appears to be well mixed with the molecular material and may be the interclump gas. The nearby H II regions S280 and S282 appear to be unrelated to the molecular complex. The complex seems to be another example of a region where sequential star formation has taken place, but the most commonly discussed triggering mechanisms do not seem to be responsible for the most recent star formation. We note that the implosion of dense clumps may be an important mechanism for forming massive stars.

There are three particularly interesting regions in the molecular cloud. The strongest CO peak (A1-1) shows no evidence of star formation, but may represent the very earliest stages of the formation process. We suspect that it may be a far infrared source. The Ear is an apparently expanding shell of dust and gas from which small clumps of CO may have been ejected. There is no obvious source for the expansion, however. Cloud IRS possesses an embedded infrared source (GL-961) which is centered on an unusual self-reversed CO line profile. The profile indicates that the cloud as a whole is expanding and the expansion is consistent with the rate of energy input from the infrared source.

APPENDIX A

EQUIPMENT AND OBSERVING TECHNIQUES

The 1.2 m telescope at Columbia University has a resonant ring diplexer designed and built by A. R. Kerr and a Ga-As Schottkey barrier diode mixer (Cong *et al.* 1979). The parameters of the telescope relevant to the observations are given in Table 1.

Incoming signals were corrected for atmospheric attenuation by the chopper wheel technique of Penzias and Burrus (1973) modified by Davis and Vanden Bout (1973) for a double-sideband receiver. The atmospheric opacity was calculated according to the two-layer model of Kutner (1978), and was measured by an antenna dipping prior to each observing session. Before each integration, a 5 s calibration was performed. The entire calibration procedure was checked by monitoring the intensity of the Orion A peak at least once per observing session. The integration time for each position observed was set so that the rms noise was ~0.3 K. This ensured that a 1 K line would be observable, and was generally achieved with 2 to 5 minute integrations depending on the source elevation and the weather.

In order to attain higher spatial and frequency resolution, selected areas were observed using the 5 m telescope at the MWO. The telescope parameters are given in Table 1. Observations were made at the frequencies of CO, ^{13}CO, and 2 mm H_2CO. The single-sideband noise temperature of the system at CO frequencies was usually ~1800–2000 K and was 1500 K at the H_2CO frequency. Calibrations of 30 s were performed in a manner similar to the one used at the 1.2 m telescope except that they were less frequent. The atmospheric opacity was determined from a single-layer plane-parallel model of the atmosphere. On-source integrations were 5 minutes at each position, usually resulting in rms noise temperatures of ~05–0.8 K. The resulting signal-to-noise ratio was comparable to that obtained at the 1.2 m telescope because filter and beam dilution at the smaller dish made the lines appear weaker.

In the most interesting regions of the Rosette molecular complex, still higher spatial and frequency resolutions of CO and ^{13}CO was obtained with the 11 m NRAO telescope at Kitt Peak, the parameters of which are given in Table 1. Calibration of the data uses the technique described by Ulich and Haas (1976). Typical rms noise temperatures for the 100 kHz observations was typically 0.7 K with 5 minute on-source integrations.

APPENDIX B

THE EXTENT OF THE MOLECULAR COMPLEXES

Significant amounts of gas below the sensitivity limit of the observations (1 K-MHz) could seriously affect our estimates of the extent of the emission and the molecular mass related to each complex. We have therefore estimated the amount of undetected gas (below an antenna temperature of 1 K-MHz) by extrapolating from the lowest intensities observed in each complex.

The area within each contour of the maps of velocity integrated intensity was measured with a planimeter (measurement accuracy and repeatability for the lowest contours was better than 1%). The logarithm of the area is plotted as a function of integrated antenna temperature for each complex in Figure 14. The plots show that for each complex, the lowest three or four contours fall on a straight line. A linear extrapolation to zero intensity is given in each case. Table 6 gives the percentage increase in the area for each large cloud.

Table 6 implies that if each complex were observed at an arbitrarily high sensitivity, the average linear dimension of each complex would increase by no more than ~20%. This in turn implies that the complexes probably have well-defined boundaries, and that the interface between the complexes and the less dense phase of the interstellar medium is fairly sharp. This inference is strengthened by observations at a few positions several beamwidths outside the lowest detected contour at sensitivity of ~0.2 K. In no case was any emission found. This result is not surprising in view of the close correspondence between the extinction and the extent of the CO emission (cf. the relevant maps for each complex).

An interesting feature of Figure 14 is that the slope of the line defined by the lowest contours is relatively constant from complex to complex. The area within the lowest contours is related to the integrated temperature according to equation (1) (§ II*b*). The constancy of the slope defined by the contours $\lesssim 4$ K-MHz may be indicative of a fundamental property of OB molecular complexes. It would be interesting to see whether the same proportionality holds for other OB molecular complexes and for smaller molecular clouds as well.
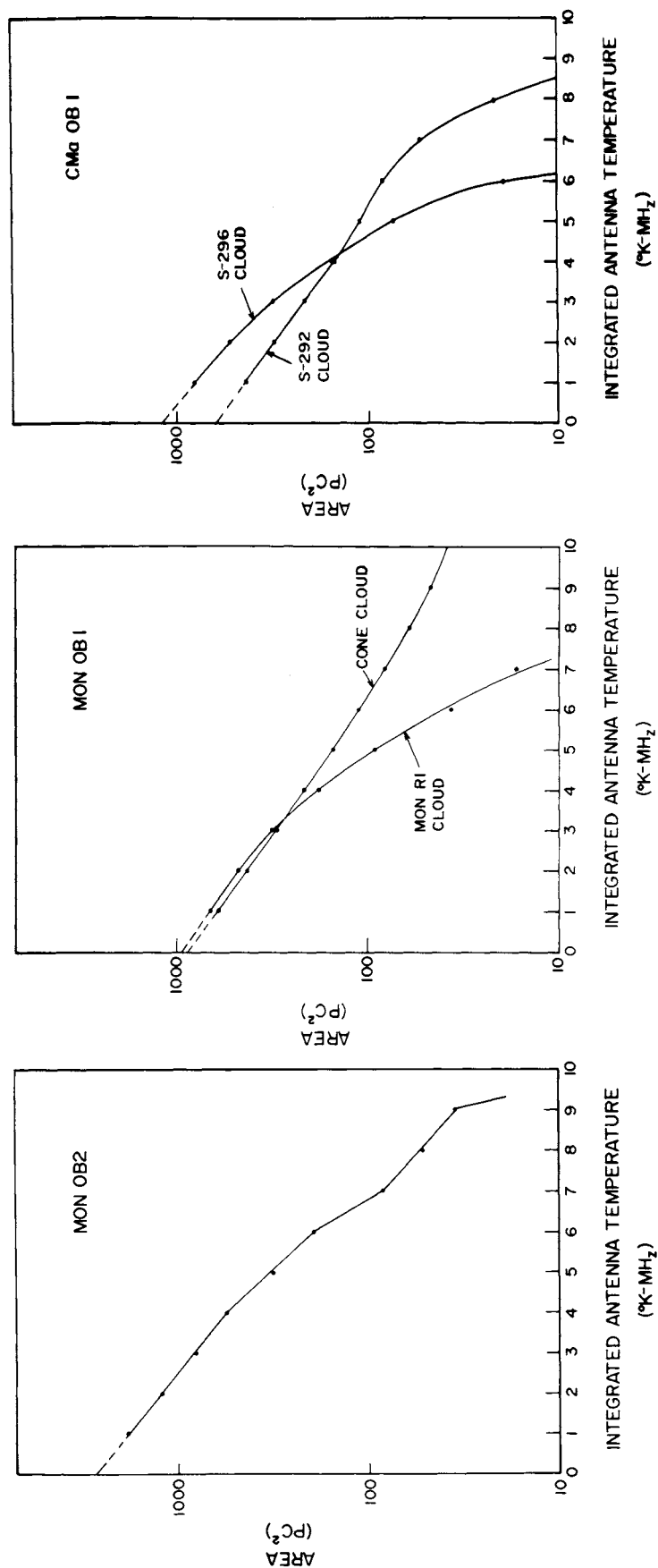
FIG. 14.— Plots of the area within a given CO contour as a function of integrated antenna temperature for the three molecular complexes which are the subject of this series of papers. The dotted line is a linear extrapolation to zero intensity.

TABLE 6

INCREASE IN APPARENT CLOUD AREA FROM EXTRAPOLATION TO
ZERO INTENSITY

Source	% Increase
Mon OB2..........................	50
Mon OB1:	
Cone cloud	43
Mon R1 cloud....................	40
CMa OB1:	
S-292 cloud	46
S-296 cloud	51

APPENDIX C

MASS ESTIMATES

The masses of the molecular complexes are estimated from the CO observations, but because the method of estimation requires assumptions about unobserved quantities, the final values are uncertain by at least a factor of 2. However, the *relative* masses of the complexes are probably accurately determined since this series of papers presents a consistent set of observations analyzed in the same way. It will be shown in the final paper in this series that the total molecular mass in each complex is very nearly the same. The similarity in the mass estimates is therefore indicative of a real similarity in the masses, not merely a chance coincidence related to the method of estimation.

Where ^{13}CO has been observed, the column densities have been calculated using ^{13}CO as a tracer for the molecular hydrogen gas. The ^{13}CO column density $N(^{13}CO)$ is calculated from observations of the CO and ^{13}CO lines under the assumption that all the CO is in local thermodynamic equilibrium (LTE). The H_2 column density $N(H_2)$ is obtained by assuming that there is a constant ratio of $N(^{13}CO)/N(H_2)$; the value of this ratio is determined from observations of small diffuse molecular clouds (Dickman 1978). The constancy of this ratio and the assumption of LTE are the two central assumptions of the method.

$N(H_2)$ was calculated for each position toward which ^{13}CO was observed from equations (C1)–(C4):

$$N(H_2) = 5 \times 10^5 N(^{13}CO),$$ (C1)

$$N(^{13}CO) = 2.42 \times 10^{14} \frac{\tau_{13} \Delta V T_x}{1 - \exp(-5.29/T_x)},$$ (C2)

$$\tau_{13} = -\ln\left[1 - \frac{T_L^{13}}{5.29}\left\{[\exp(5.29/T_x) - 1]^{-1} - 0.164\right\}^{-1}\right],$$ (C3)

$$T_x = 5.33\left[\ln\left(1 + \frac{5.53}{T_L^{12} + 0.819}\right)\right]^{-1},$$ (C4)

where T_L^{12} is the CO line antenna temperature in kelvins, T_L^{13} is the ^{13}CO line antenna temperature in kelvins, ΔV is the line width (FWHM) of the ^{13}CO line in km s^{-1}, T_x is the excitation temperature in kelvins, and τ_{13} is the ^{13}CO optical depth. The mass derived from the product of $N(H_2)$ and the projected surface area is the directly observed mass M_{OBS} of a complex.

Because the ^{13}CO intensity is generally much weaker than the CO intensity in a given direction, the extent of the ^{13}CO observed is much smaller than the extent of the CO. To obtain $N(H_2)$ in the region where ^{13}CO is not observed (the CO halo), values of the ^{13}CO line intensities are assumed from the CO observations. The mean ^{13}CO optical depth $\langle\tau_{13}\rangle$ was calculated for each complex (Mon OB1 and CMa OB1 are composed of two large clouds; $\langle\tau_{13}\rangle$ was calculated separately for each). It was assumed that $\langle\tau_{13}\rangle$ has the same value in the remainder of the complex. Because $\tau_{13} \approx T_L^{13}/T_L^{12}$, the assumption is equivalent to assuming that the ratio of the strength of the CO line to the ^{13}CO line has some constant value in the CO halo. The mass thus obtained is designated M_{HALO}.

To estimate the unseen mass below the sensitivity limit of the observations (M_{UNS}), we use the values in Table 6 to obtain the projected surface area of CO below the limit of detectability. The mean column density of H_2 in this region is obtained by assuming that the mean CO antenna temperature is 0.5 K, and that $\langle\tau_{13}\rangle$ in this region has the same value as in the CO halo. The correction for unseen mass is ~20% of the total estimated mass ($M_{COMP} = M_{OBS} + M_{HALO} + M_{UNS}$) in each case.

CORRECTIONS AND UNCERTAINTIES

The first correction to the mass estimates determined from observations at the 1.2 m telescope results from the combined effects of channel dilution and the nonlinearity of equations (C2)–(C4). If a source is observed with a telescope which does not fully resolve a given spectral line in frequency, the peak intensity will be smaller and the line width larger than what would be observed if the line were fully resolved. Because the integrated intensity $\int T_A(v)\,dv$ is conserved for a Gaussian line, the relative decrease in the peak intensity of the line is the same as the relative increase in the line width. Equation (C2), however, is more strongly dependent on the intensity of a (CO) line than it is on the (^{13}CO) line width. The lines observed with the 1.2 m telescope tend to be underresolved, and comparisons over large areas with results from the 5 m telescope indicate that corrections to $N(^{13}$CO) range from 10% to 60% with a typical correction of 35%. All of the column densities and masses determined from observations with the 1.2 m telescope include a 35% correction for the effects of channel dilution.

The largest uncertainty in the mass estimates comes from the assumption of a constant $N(\mathrm{H_2})/N(^{13}$CO) ratio. We adopt a value of 5×10^5 for this ratio from the work of Dickman (1978). Dickman quotes a statistical uncertainty of $\pm 50\%$ in his work, and this should be considered to be the minimum uncertainty in the total mass estimates.

Dickman's result show a relation between $N(^{13}$CO) and A_v which is linear to 1.0×10^{16} cm^{-2}. As pointed our by Blitz and Shu (1980), this implies that within the linear regime, the CO observations should give reliable values of $N(\mathrm{H_2})$ within the statistical uncertainties. Dickman derived $N(^{13}$CO) from direct observations of T_L^{12}, T_L^{13} and ΔV, $N(\mathrm{H_2})$ was derived from star counts calibrated by the generally accepted gas to extinction ratio of Jenkins and Savage (1974). Dickman's results are therefore an *empirically derived* relation between a particular function of T_L^{12}, T_L^{13}, ΔV (defined by eqs. [3]–[5]), and $N(\mathrm{H_2})$. Regarded in this fashion, the empirical relation is free of *any* theoretical assumptions, and may be applied with confidence as long as there are no systematic differences between the giant complexes and the clouds of Dickman's sample.

For values of $N(^{13}$CO) $> 1.0 \times 10^{16}$ cm^{-2}, however, Dickman generally gives only lower limits to A_v [i.e., $N(\mathrm{H_2})$], and $N(\mathrm{H_2})/N(^{13}$CO) may be considerably higher in this regime (due to depletion onto grain surfaces, for example). We correct for this uncertainty by calculating the fraction, f_{CORE}, of each complex by mass where $N(^{13}$CO) $> 1.0 \times 10^{16}$ cm^{-2}. The value of f_{CORE} is < 0.18 for any one complex. In the high-density regions, we assume that $N(\mathrm{H_2})/N(^{13}$CO) $= 2 \times 10^6$, a value derived by fitting observed CO line profiles in the cores of dense molecular clouds to the large velocity gradient model (e.g., Solomon and Sanders 1979). This correction increases the mass estimate by no more than $\sim 60\%$ for any one complex. The final adopted masses for all of the complexes is M_{TOT} which contains the correction for channel dilution and higher $N(\mathrm{H_2})/N(^{13}$CO) in the cores of the complexes.

REFERENCES

Becklin, E. E., Neugebauer, G., and Wynn-Williams, C. G. 1973, *Ap. J. (Letters)*, **182**, L7.
Blaauw, A. 1964, *Ann. Rev. Astr. Ap.*, **2**, 213.
Blitz, L. 1978, Ph.D. dissertation, Columbia University.
Blitz, L., Fich, M., and Stark, A. A. 1979, in *IAU Symposium 87, Interstellar Molecules*, ed. B. Andrew (Dordrecht: Reidel), in press.
Blitz, L., and Lada, C. J. 1979, *Ap. J.*, **227**, 152.
Blitz, L., and Shu, F. H. 1980, *Ap. J.*, **238**, 148.
Bottinelli, L., and Gouguenheim, L. 1964, *Ann. d'Ap.*, **27**, 685.
Burton, W. B., Liszt, H. S., and Baker, P. L. 1978, *Ap. J. (Letters)*, **219**, L67.
Cohen, M. 1973, *Ap. J. (Letters)*, **185**, L75.
Cong, H. I., Kerr, A. R., Thaddeus, P., and Mattauch, R. J. 1979, *IEEE Trans., M.T.T.*, **27**, 245.
Courtès, G., Cruvellier, P., and Georgelin, Y. 1966, *J. d'Obs.*, **49**, 329.
Davis, J. H., and Vanden Bout, P. 1973, *Ap. Letters*, **15**, 43.
Dickel, H. R., Dickel, J. R., Wilson, W. J., and Pomphrey, R. B. 1975, *Bull. AAS*, **7**, 556.
Dickman, R. L. 1978, *Ap. J. Suppl*, **37**, 407.
Dyson, J. E. 1973, *Astr. Ap.*, **23**, 381.
Elmegreen, B. G., and Lada, C. J. 1977, *Ap. J.*, **214**, 725.
Encrenaz, P. J., Falgarone, E., and Lucas, R. 1975 *Astr. Ap.*, **44**, 73.
Fountain, W. F., Gary, G. A., and O'Dell, C. R. 1979, *Ap. J.*, **229**, 971.
Harris, S. 1976, *M.N.R.A.S.*, **174**, 601.
Harvey, P. M., Campbell, M. F., and Hoffman, W. F. 1977, *Ap. J.*, **215**, 151.
Herbig, G. H. 1974, *Pub. A. S. P.*, **86**, 604.
Hutchings, J. B. 1976, *Ap. J.*, **203**, 438.
Jenkins, E. B., and Savage, D. B. 1974, *Ap. J.*, **187**, 243.

Johnson, H. L. 1962, *Ap. J.*, **136**, 1135.
Kippenhahn, R., and Smith, L. 1969, *Astr. Ap.*, **1**, 142.
Kirschner, R. P., Gull, T. R., and Parker, R. A. R. 1978, *Astr. Ap. Suppl.*, **31**, 261.
Knapp, G. R., Kuiper, T. B. H., Knapp, S. L., and Brown, R. L. 1976, *Ap. J.*, **206**, 443.
Kutner, M. L. 1978, *Ap. Letters*, **19**, 81.
Kutner, M. L., and Tucker, K. D. 1975, *Ap. J.*, **199**, 79.
Kutner, M. L., Tucker, K. D., Chin, G. C., and Thaddeus, P. 1977, *Ap. J.*, **215**, 521.
Kwan, J., and Scoville, N. Z. 1976, *Ap. J. (Letters)*, **210**, L39.
Lada, C. J. 1980, in *Giant Molecular Clouds in the Galaxy*, ed. P. M. Solomon and M. G. Edmunds (Oxford: Pergamon), in press.
Leung, C. M., and Brown, R. L. 1977, *Ap. J. (Letters)*, **214**, L73.
Loren, R. B. 1976, *Ap. J.*, **209**, 466.
Mathews, W. G. 1966, *Ap. J.*, **144**, 206.
————. 1967, *Ap. J.*, **147**, 965.
Menon, T. K. 1962, *Ap. J.*, **135**, 394.
Miller, G. E., and Scalo, J. M. 1978, *Pub. A. S. P.*, **90**, 506.
Miller, J. S. 1968, *Ap. J.*, **151**, 473.
Milman, A. S., Knapp, G. R., Knapp, S. L., and Wilson, W. J. 1975, *A. J.*, **80**, 101.
Minkowski, R. 1949, *Pub. A. S. P.*, **61**, 151.
Morgan, W. W., Hiltner, W. A., Neff, J. S., Garrison, R., and Osterbrock, D. E. 1965, *Ap. J.*, **142**, 974.
Penzias, A. A., and Burrus, C. 1973, *Ann. Rev. Astr. Ap.*, **11**, 51.
Raimond, E. 1966, *B. A. N.*, **18**, 191.
Riddle, R. K. 1972, Ph.D. dissertation, University of Maryland.
Roberts, M. S. 1957, *Pub. A. S. P.*, **69**, 59.
Sargent, A. I. 1977, *Ap. J.*, **218**, 736.
Schneps, M. H., Ho, P. T. P., and Barrett, A. H. 1980, *Ap. J.*, submitted.

Simon, T., Simon, M., and Joyce, R. R. 1979, *Ap. J.*, **230**, 127.
Smith, M. G. 1968, *Ap. Space Sci.*, **1**, 68.
_____. 1973, *Ap. J.*, **183**, 111.
Snell, R. L., and Loren, R. B. 1977, *Ap. J.*, **211**, 122.
Solomon, P. M., and Sanders, D. 1979, in *Giant Molecular Clouds in the Galaxy*, ed. P. M. Solomon and M. G. Edmunds (Oxford: Pergamon), p. 41.
Spitzer, L. 1978, *Physical Processes in the Interstellar Medium* (New York: Wiley Interscience).
Stothers, R. 1972, *Ap. J.* **175**, 431.
Thaddeus, P. 1977, in *IAU Symposium* 75, *Star Formation*, ed. T. deJong and A. Maeder (Dordrecht: Reidel), p. 37.
Turner, B. E. 1969, *A. J.*, **74**, 985.

_____. 1974, in *Galactic and Extragalactic Radio Astronomy*, ed. G. L. Verschuur and K. J. Kellerman (New York: Springer), p. 199.
Turner, D. G. 1976, *Ap. J.*, **250**, 65.
Ulich, B. L., and Haas, R. W. 1976, *Ap. J. Suppl.*, **30**, 247.
Wannier, P. G., and Phillips, T. G., 1977, *Ap. J.*, **215**, 796.
Werner, M. W., Becklin, E. E., and Neugebauer, A. 1977, *Science*, **197**, 723.
Zuckerman, B., Buhl, D., Palmer, P., and Snyder, L. E. 1970, *Ap. J.*, **160**, 545.
Zuckerman, B., Kuiper, T. B. H., Rodriguez-Kuiper, E. N. 1976, *Ap. J.* (*Letters*), **209**, L137.

LEO BLITZ: Radio Astronomy Laboratory, University of California, Berkeley, CA 94720

PATRICK THADDEUS: Goddard Institute for Space Studies, 2880 Broadway, New York, NY 10025
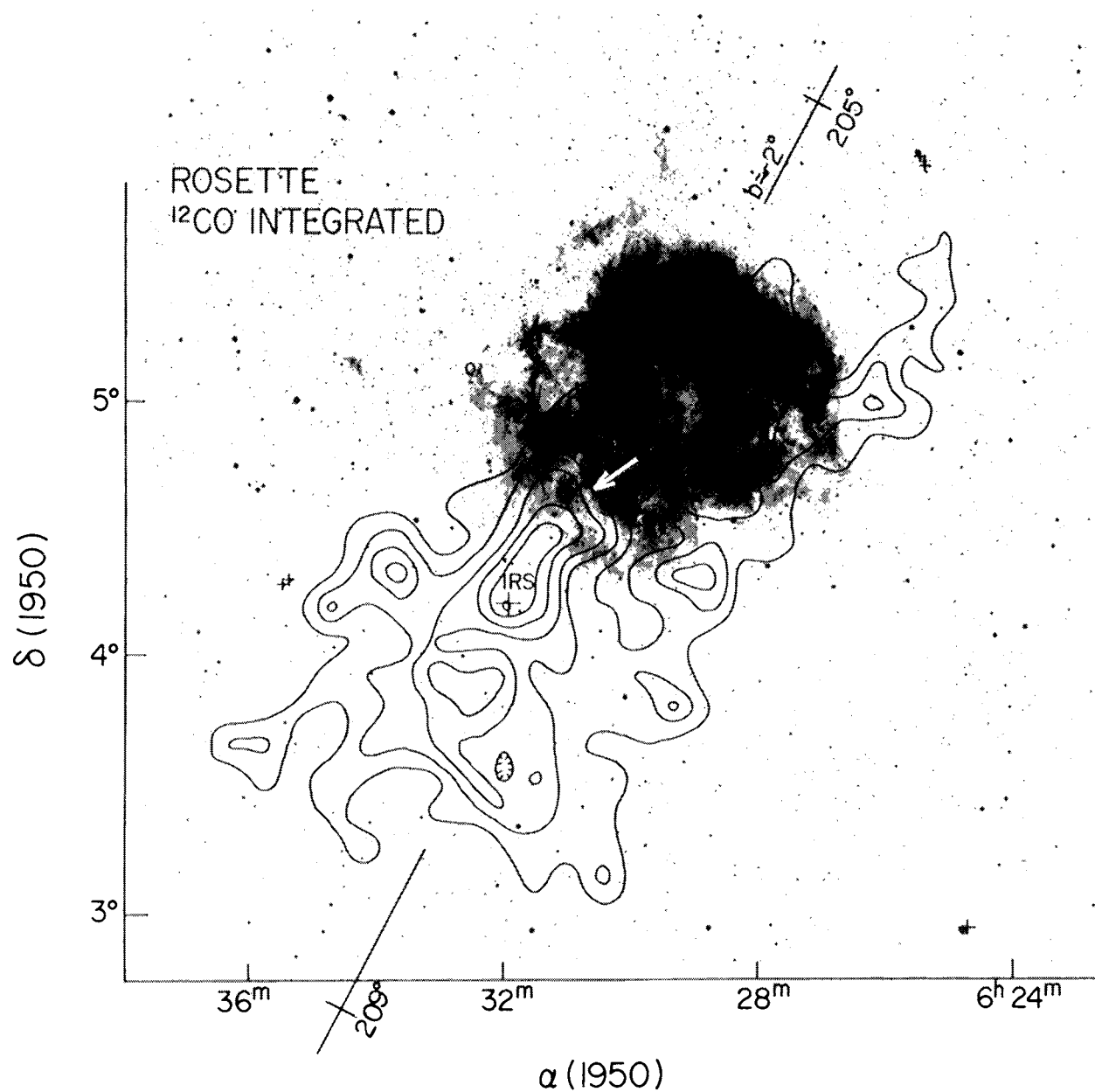
PLATE 9

FIG. 1.—Map of the integrated CO emission from Mon OB2 superposed on the red POSS plate of the region. The broken line is the line of constant galactic latitude at $b = -2$; the galactic longitude is also indicated. The arrow marks the position of the Mon ridge discussed in the text. The lowest contour is 1 K-MHz, and the contour interval is 2 K-MHz. The faint emission to the north and east of the Rosette Nebula is the Monoceros Loop supernova remnant.

BLITZ AND THADDEUS (*see* page 677)

PLATE 10
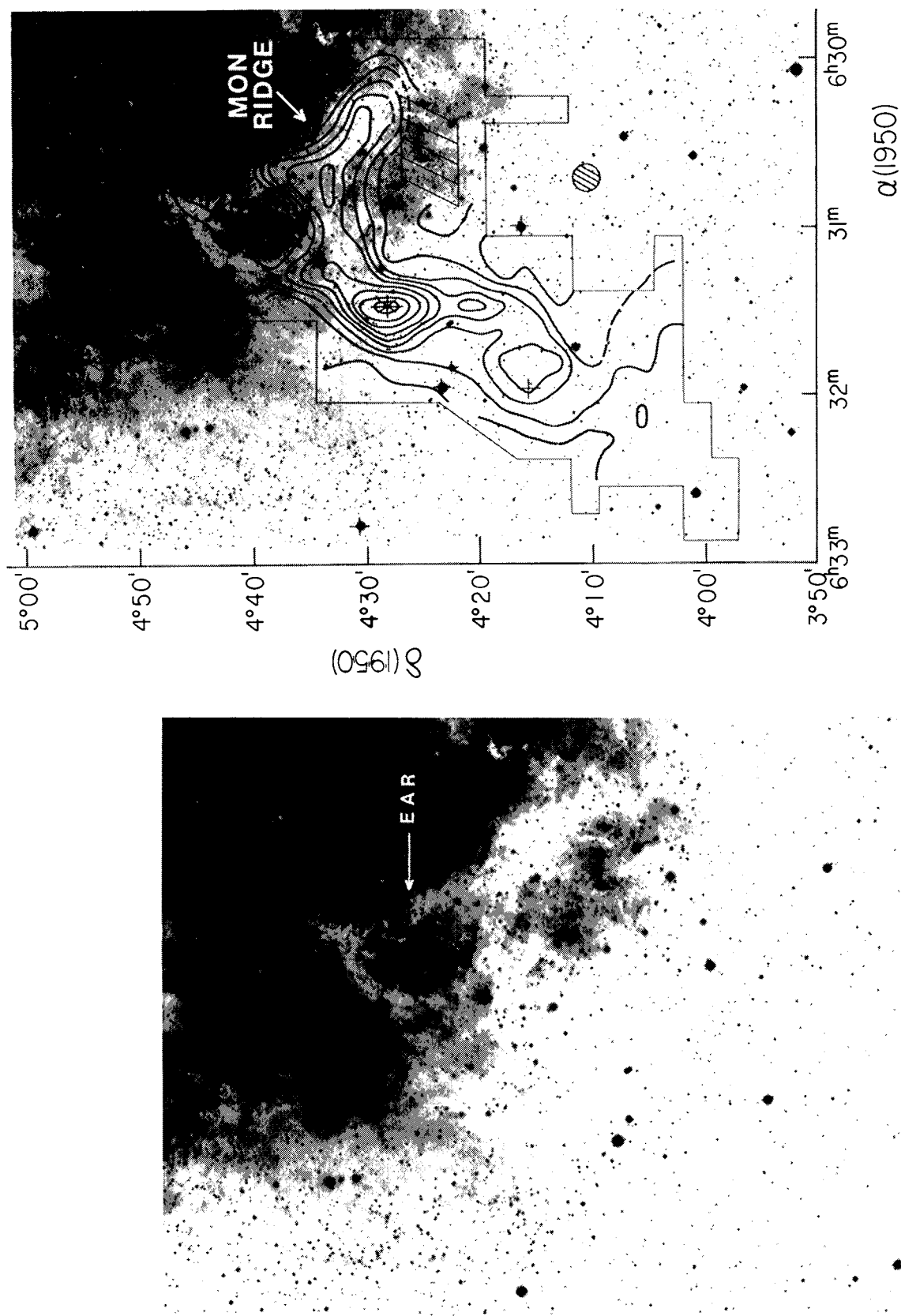
Fig. 8b

Fig. 8a

Fig. 8.—(a–f) The relationship between the optical and molecular emission in the region corresponding to Fig. 6. Fig. 8a is a detail from the red POSS plate of the region. The feature marked "Ear" refers to the dark dust lanes which resemble the outline of an ear. In Fig. 8b, Fig. 6 is superposed on the detail. In Figs. 8c–8f, the emission from spectrometer channels the LSR velocity of which is given in the upper left of each figure is also superimposed on the detail. Note the close correspondence and the variation of the CO emission and the dark material in the Ear and at various velocities.

Blitz and Thaddeus (see page 682)
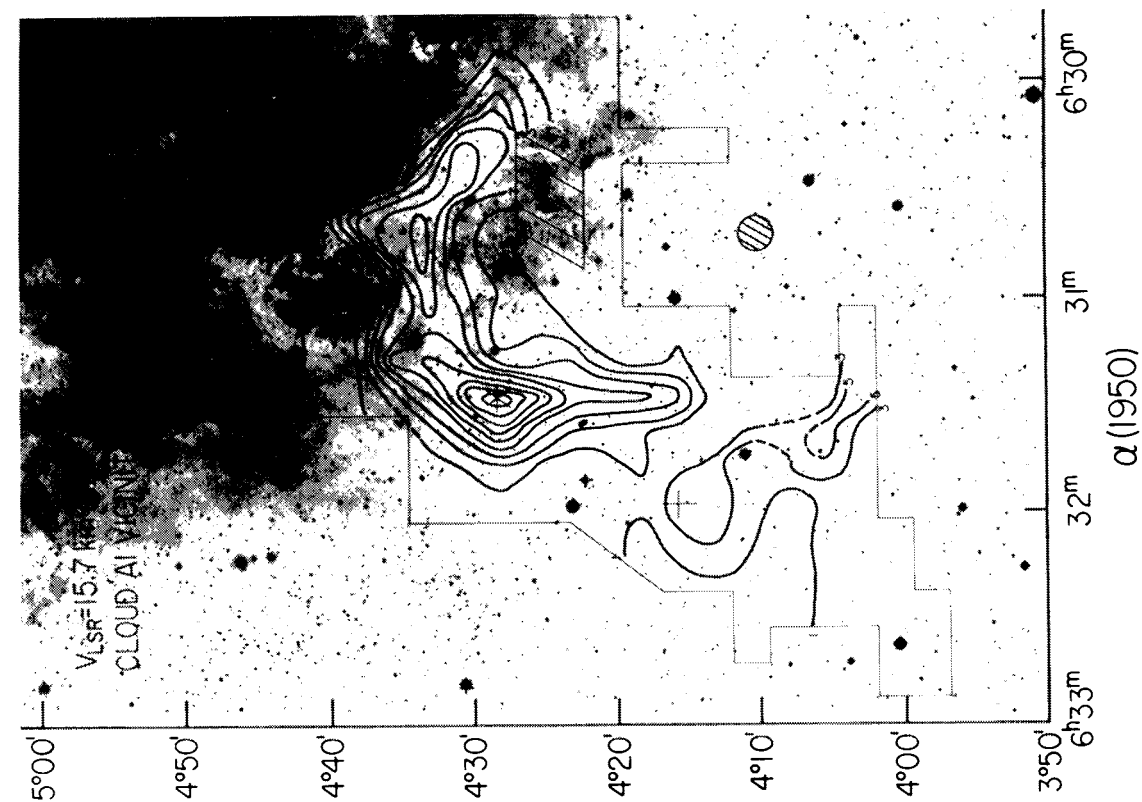
PLATE 11

FIG. 8d

FIG. 8c

BLITZ AND THADDEUS (*see* page 682)

PLATE 12

$V_{LSR} = 10.3$ KM/S
CLOUDS A2 AND B1

FIG. 8f

α (1950)

δ (1950)

$V_{LSR} = 12.3$ KM/S
CLOUDS A4 AND B1

FIG. 8e

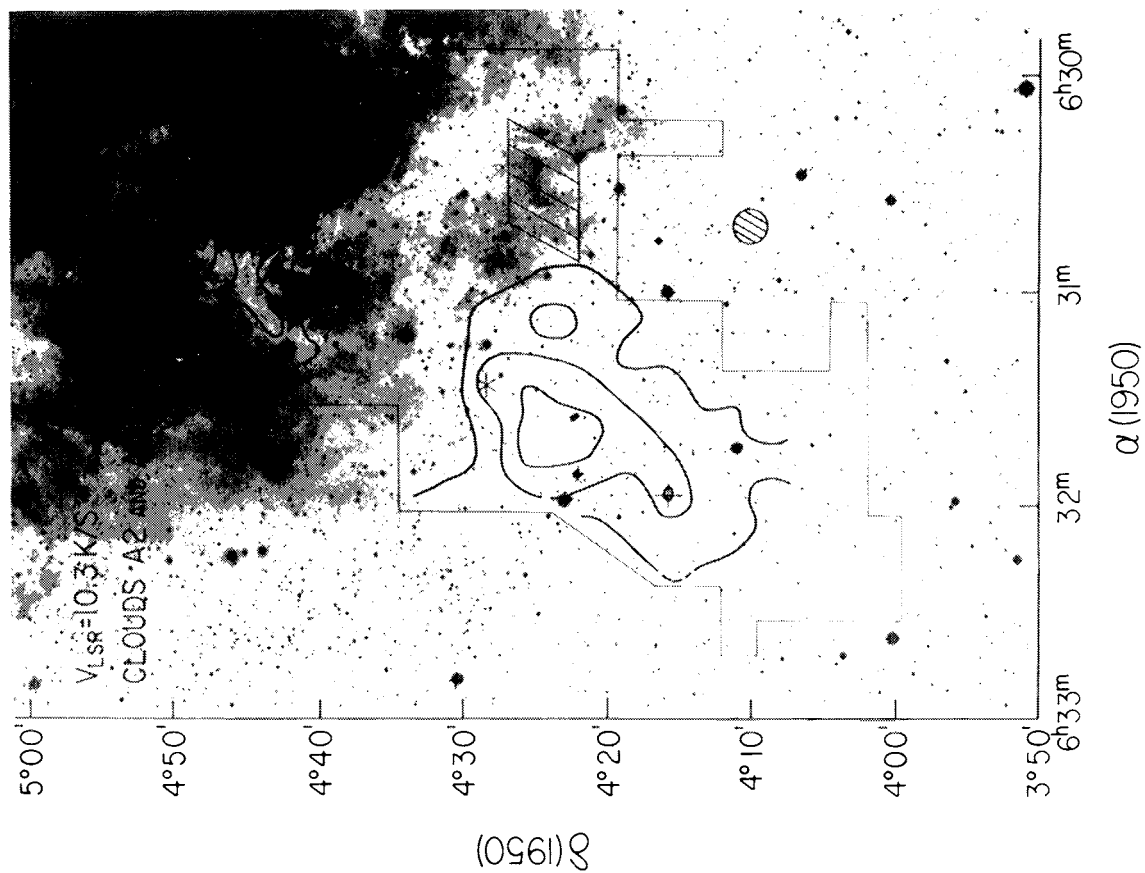α (1950)
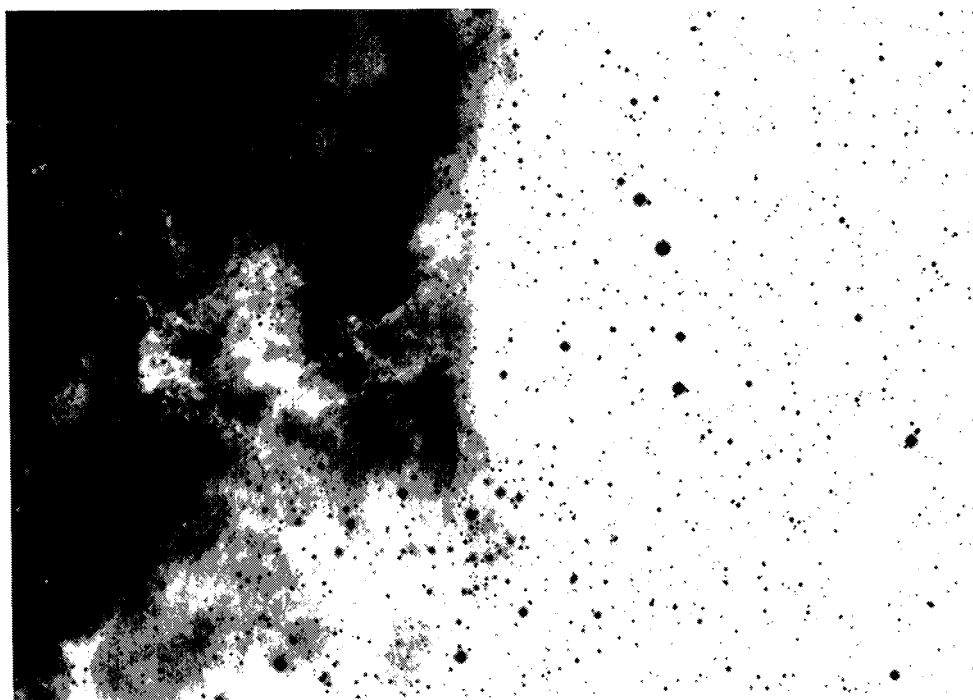
δ (1950)
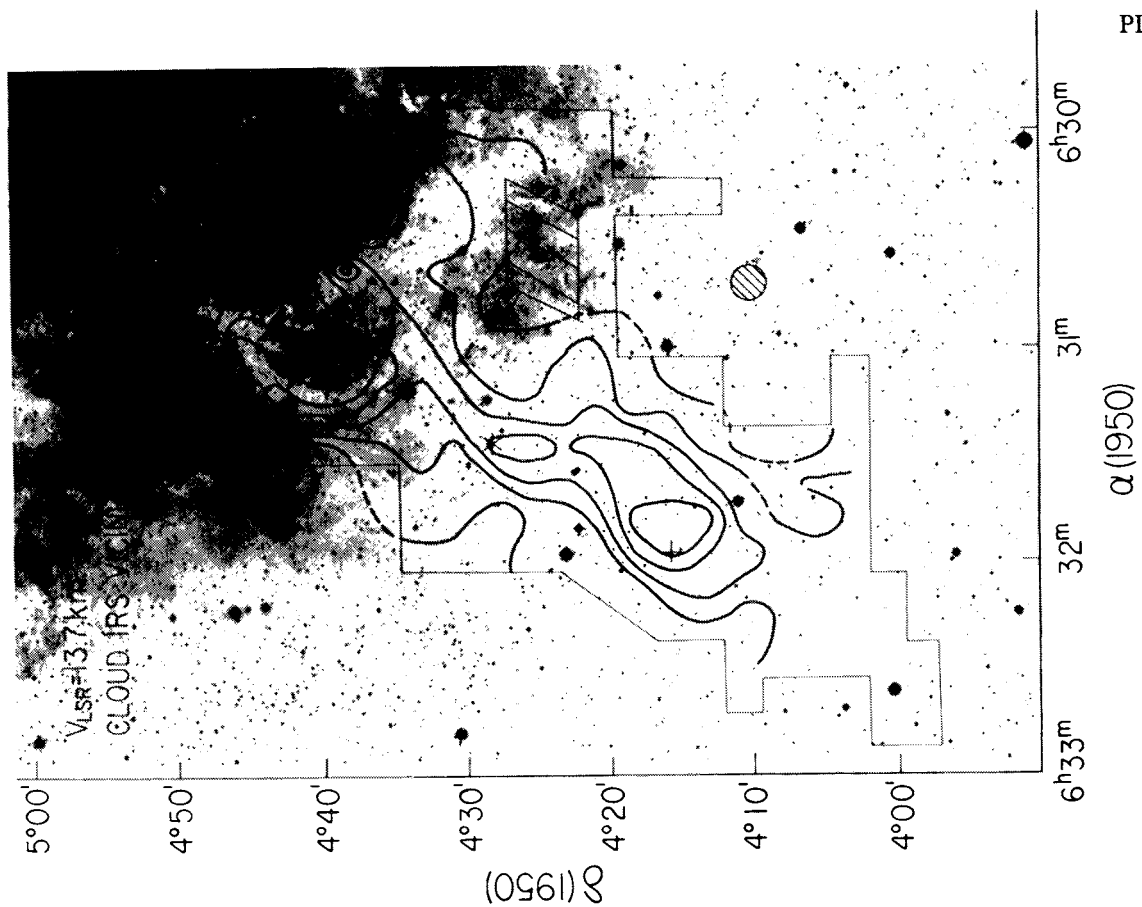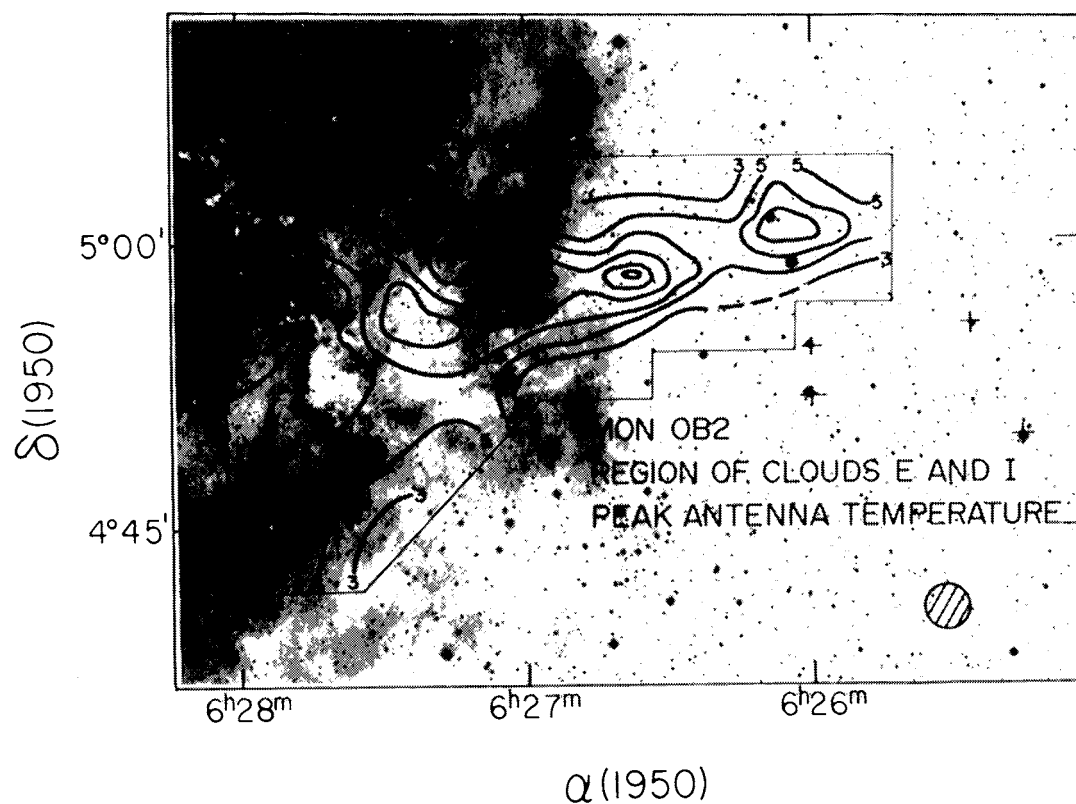
BLITZ AND THADDEUS (see page 682)

PLATE 13
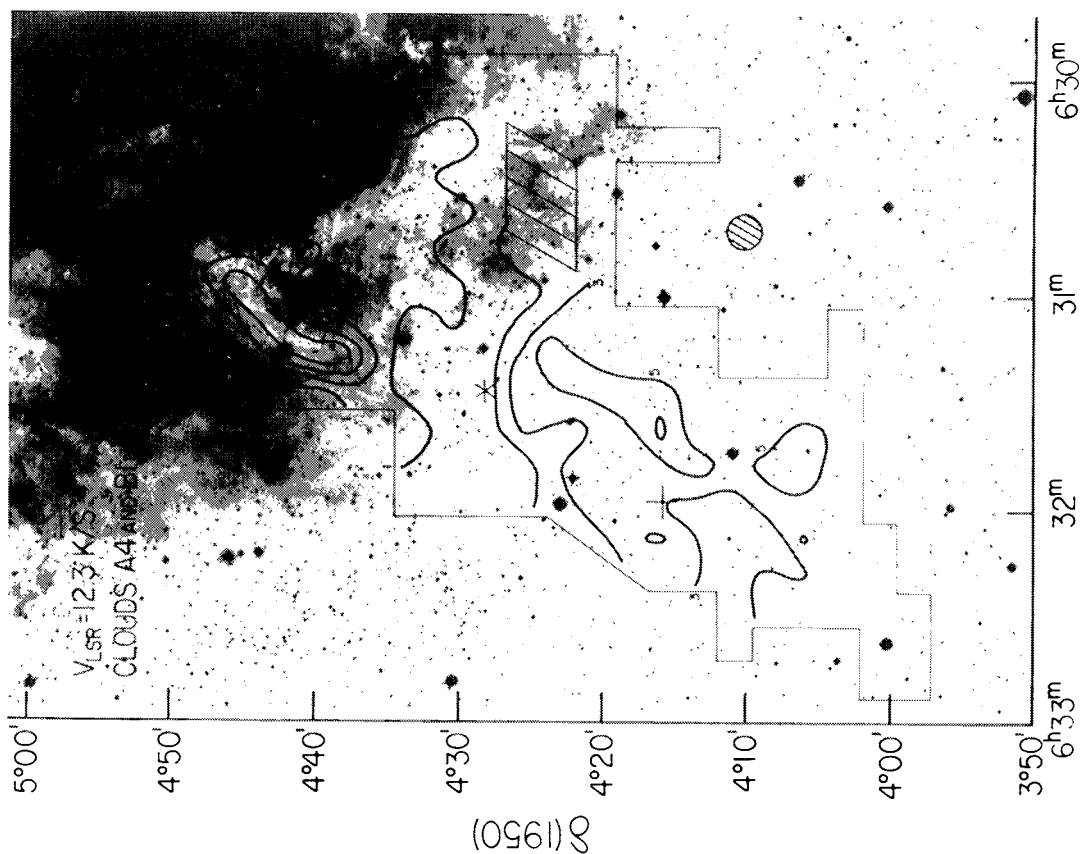
FIG. 12a

FIG. 12b

FIG. 12.—a–e The relationship between the optical and molecular emission in the "Arm." Fig. 12a is a detail from the red POSS plate of the region. Fig. 12b–12e show the CO emission observed with the 5 m telescope superposed on the detail.

BLITZ AND THADDEUS (see page 686)

CLOUDS E1 AND E2
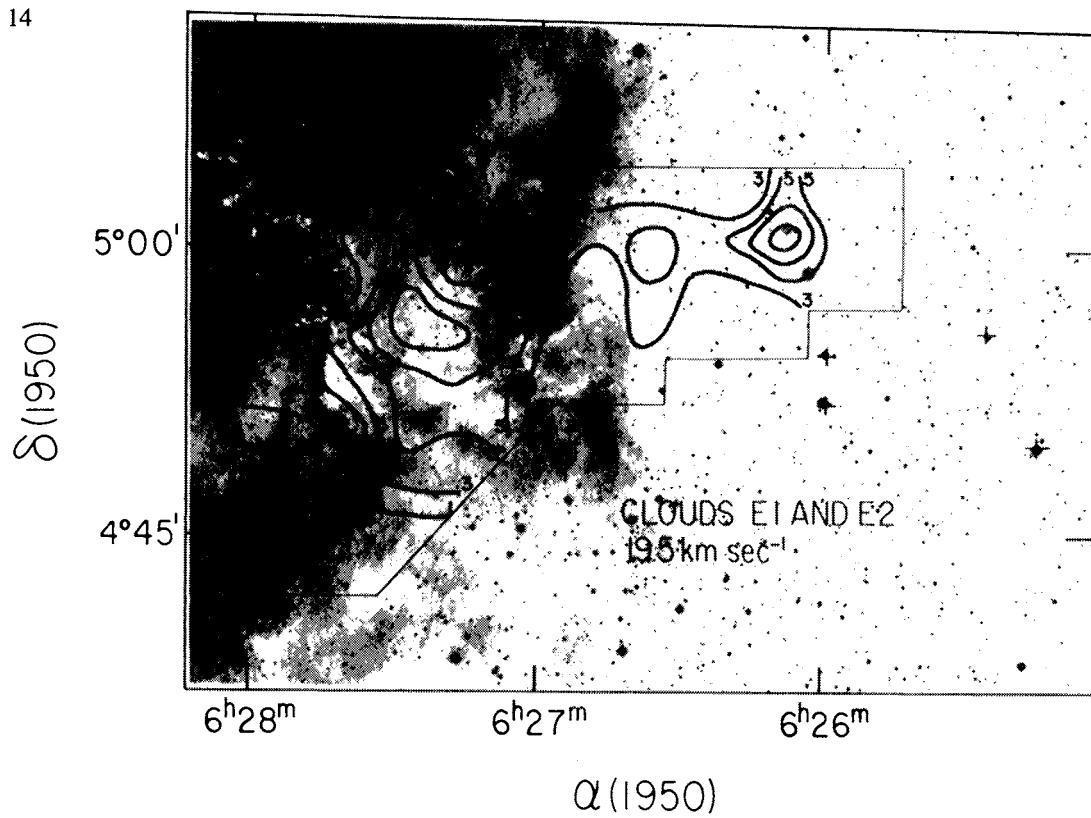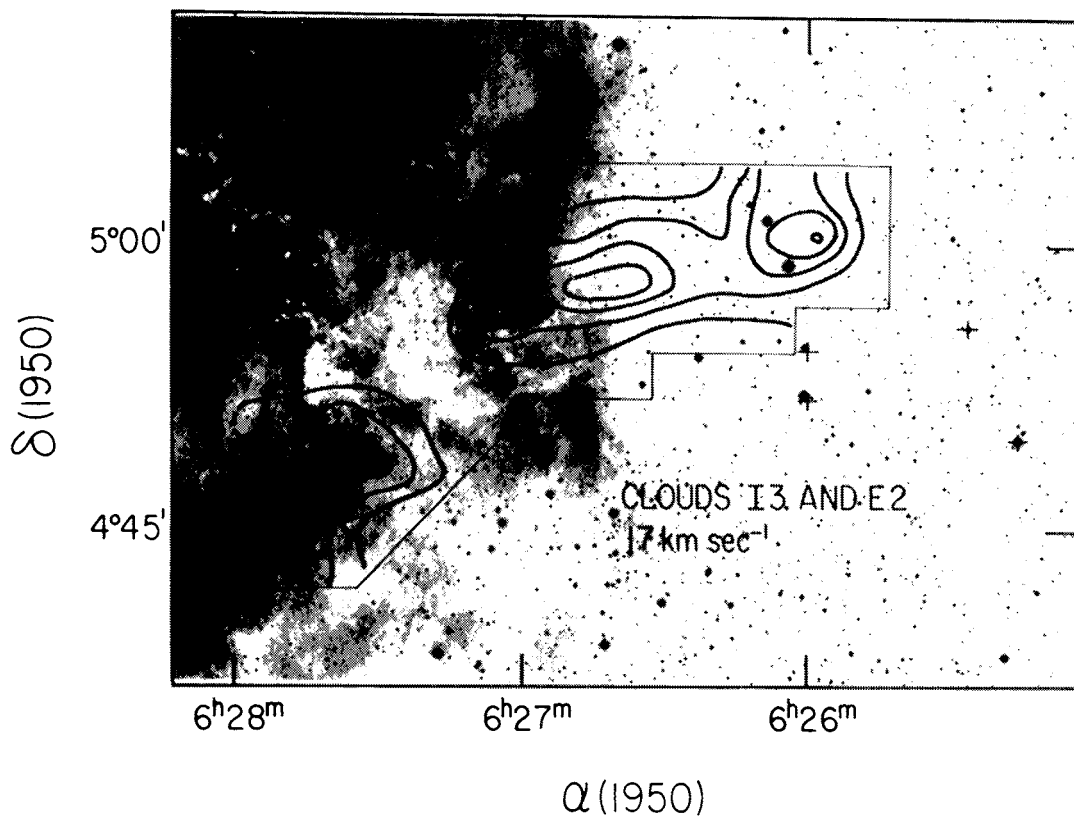19.5 km sec⁻¹

δ (1950)

α (1950)

Fig. 12c

CLOUDS E3 AND E2
17 km sec⁻¹

δ (1950)

α (1950)

Fig. 12d

PLATE 15

CLOUD II
15 km sec⁻¹

δ(1950)

5°00'

4°45'

6ʰ28ᵐ   6ʰ27ᵐ   6ʰ26ᵐ

α(1950)

FIG. 12e

BLITZ AND THADDEUS (*see* page 685)